1995ApJ...444..129G

THE ASTROPHYSICAL JOURNAL, 444:129–145, 1995 May 1

INFRARED IMAGING AND SPECTROSCOPY OF NGC 7469

R. GENZEL, L. WEITZEL, L. E. TACCONI-GARMAN, M. BLIETZ, M. CAMERON, A. KRABBE, AND D. LUTZ
Max-Planck-Institut für Extraterrestrische Physik (MPE), Postfach 1603, D-85740 Garching, Germany

AND

A. STERNBERG
School of Physics and Astronomy, Tel Aviv University, Ramat-Aviv 69978, Israel
Received 1994 July 29; accepted 1994 November 7

ABSTRACT

As part of an extensive study of the infrared properties of luminous galactic nuclei we report here subarcsecond-resolution near-infrared imaging and spectroscopy of the nucleus of the Seyfert 1 galaxy NGC 7469. Our measurements elucidate for the first time the spatial distribution of the near-infrared continuum and a number of bright near-infrared lines (Brγ, [Fe II], [Si VI], H_2, He I, and CO) on a scale of less than a few hundred parsecs. We find that these tracers originate from three distinct components: the nucleus, a 1″.5 (480 pc) radius circumnuclear ring/spiral-arm system with embedded knots, and a 1″ ridge of blueshifted, radially streaming gas emanating southward from the nucleus.

The circumnuclear ring is the location of a powerful starburst deeply embedded in a large concentration of molecular gas and dust and has a luminosity of $\approx 3 \times 10^{11}\ L_\odot$, two-thirds of the bolometric luminosity of the entire galaxy. It contains a number of supergiant star formation regions with a few 10^4 OB stars each. Our 0″.4 resolution near-infrared images do not show evidence for a stellar bar. Gas influx into the nucleus and starburst ring were most likely triggered $\geq 10^8$ yr ago by the interaction of NGC 7469 with its neighbor, IC 5283.

A comparison of the mass derived from gas and stellar dynamics and from the CO 1–0 millimeter line emission suggests that the conversion factor from molecular hydrogen column density to integrated CO flux $[X = N(H_2)/I(CO)]$ in the central 800 pc is significantly smaller than in the Galactic disk, presumably as the result of the impact of the intense star formation activity on the surrounding interstellar medium.

We have carried out a quantitative analysis of the ring's visible, infrared, and radio emission using star cluster models. The data are well fit by two types of solutions. One possibility is that the star formation rate has been constant ($\approx 30\ M_\odot\ \mathrm{yr}^{-1}$) over the last several 10^7 yr and stars more massive than 30–40 $M_\odot$ have not been forming during this period. An alternative model that does not require an upper mass cutoff is a decaying burst with a decay time significantly less than its present age ($\approx 1.5 \times 10^7$ yr). For both star formation histories and for the small $N(H_2)/I(CO)$ conversion factor mentioned above, the star formation efficiency in NGC 7469 is high and the burst is soon going to end because the gas reservoir is exhausted.

Our 2.1 μm H_2 $S(1)$ line maps show that there is a large concentration of molecular gas close to the Seyfert 1 nucleus of NGC 7469. The central 10^2 pc of NGC 7469 contains $10^{8\pm1}\ M_\odot$ of neutral interstellar gas, consistent with current unifying models for Seyfert 1 and 2 nuclei.

Broad (FWHM 1400 km s^{-1}) 1.96 μm [Si VI] line emission arises in moderately dense ($n_e \geq 10^2\ \mathrm{cm}^{-3}$) gas within a few 10^2 pc from the nucleus.

Our work clearly shows that NGC 7469 is a luminous Seyfert galaxy whose total energy output is predominantly powered by star formation.

Subject headings: galaxies: individual (NGC 7469) — galaxies: ISM — galaxies: nuclei — galaxies: Seyfert — galaxies: stellar content — infrared: galaxies — stars: formation

1. INTRODUCTION

The SBa Seyfert 1 galaxy NGC 7469 (Arp 298, Mrk 1514, UGC 12332) was on Seyfert's (1943) original list of galaxies with active galactic nuclei (AGNs) and has since been extensively studied in the visible, radio, and X-ray bands (e.g., Burbidge, Burbidge, & Prendergast 1963; Anderson 1973; Ulvestad, Wilson, & Sramek 1981; Heckman et al. 1986; Wilson et al. 1986, 1991; Piro, Yamauchi, & Matsuoka 1990). It is a bright infrared source with a total mid- and far-infrared luminosity of $3 \times 10^{11}\ L_\odot$ [for an assumed distance of 66 Mpc, derived from $H_0 = 75$ km s^{-1} Mpc^{-1} and v_{hel} (NGC 7469) = 4930 ± 20 km s^{-1}; Heckman et al. 1986]. NGC 7469 is gas rich. About $1.5 \times 10^{10}\ M_\odot$ of molecular gas are concentrated within ≈0.8 kpc of the nucleus if the Galactic disk conversion rate from CO 1–0 millimeter line flux to molecular hydrogen column density is adopted (Meixner et al. 1990). There are several pieces of evidence which indicate that a significant fraction of the total luminosity originates from an extended (≥3″ diameter corresponding to ≥1 kpc) star-forming zone surrounding the nucleus:

1. The large (35 Jy) 100 μm *IRAS* flux and large 100 to 12 μm flux ratio (25, as compared to ∼5 for other *IRAS* Seyfert 1 galaxies; Roche et al. 1991);
2. A ≥5″ diameter region of extended [O III], Hβ, and Hα line emission (Wilson et al. 1986; Heckman et al. 1986);
3. A similar size region of extended nonthermal, radio con-

tinuum emission with several brighter knots at a distance of 1″.5–2″ from the nucleus (Ulvestad et al. 1981; Condon et al. 1982; Wilson et al. 1991);

4. A circumnuclear ring structure (radius 1″.5), seen in 5400–6700 Å continuum speckle imaging (Mauder et al. 1994) and in 11.7 μm continuum imaging (Miles, Houck, & Hayward 1994); and

5. 3.3 μm and 8–13 μm unidentified infrared emission features ascribed to polycyclic aromatic hydrocarbons (PAHs; Aitken, Roche, & Phillips 1981; Cutri et al. 1984) with about the same spatial distribution as the extended stellar, gas, and dust emission (Mazzarella et al. 1994; Miles et al. 1994).

In order to study the properties of star formation and the interstellar medium (ISM) in NGC 7469 in more detail, we have carried out a program of high spatial resolution, near-infrared imaging and spectroscopy. The measurements we discuss here were obtained with the MPE high-resolution camera SHARP on the European Southern Observatory (ESO) 3.5 m New Technology Telescope (NTT), the MPE Fabry-Perot imager FAST on the 4.2 m William Herschel Telescope (WHT), and the ESO long slit spectrometer IRSPEC on the NTT. We also present the first results of the new MPE imaging spectrometer 3D taken during its commissioning run on the 3.5 m Calar Alto telescope.

Suffering much less from dust extinction than observations in the visible waveband, measurements in the near-infrared promise a better handle on the quantitative properties of star formation in and near this AGN. For this purpose we have modeled our new infrared observations, along with relevant observations from the literature, with a starburst code (Krabbe, Sternberg, & Genzel 1994, henceforth KSG). Another goal of our infrared spectroscopy was to search for and map infrared line emission from coronal gas recently found in several other Seyfert galaxies (Oliva & Moorwood 1990; Oliva et al. 1994). In addition we wanted to investigate the spatial distribution of the 2 μm H_2 $S(1)$ line emission discovered by Heckman et al. (1986), as recent "unifying" scenarios (e.g., Antonucci 1993) propose the existence of nuclear molecular gas concentrations in all Seyfert galaxies, perhaps in the form of compact molecular "tori" (Krolik & Begelman 1986).

2. OBSERVATIONS

We have obtained ≈0″.4 resolution *J*, *H*, and *K* images of the center of NGC 7469 with the MPE high-resolution camera SHARP. We have also carried ≤1″ resolution imaging spectroscopy of a number of prominent lines between 1.6 and 2.4 μm with the MPE Fabry-Perot imager FAST and the new MPE imaging spectrometer 3D. Furthermore, we have observed several *K*-band lines with the facility spectrometer IRSPEC of ESO. In the following, we discuss the different observations in turn.

2.1. *SHARP Observations*

NGC 7469 (R.A. = $23^{\rm h}00^{\rm m}44^{\rm s}.42$, decl. = 08°36′15″.8 [1950]) was observed with the MPE 1–2.5 μm speckle camera SHARP (Hofmann et al. 1993) on the 3.5 m NTT of ESO in La Silla, Chile, in 1992 August and 1993 August. Briefly, SHARP has a 256^2 pixel NICMOS3 array with 0″.05 pixels. Data in the *J* (1.25 μm), *H* (1.65 μm), and *K* (2.2 μm) bands were taken in "rapid-guiding" mode (Genzel et al. 1994; Genzel & Eckart 1994) in ≤1″ seeing in the visible. Observations of NGC 7469 were interleaved with those of a nearby star (Yale 9212), as well as blank sky. After sky subtraction, flat-fielding, and dead pixel correction, individual seeing selected frames were recentered on the brightest pixel (the nuclear peak) and then co-added. The raw shift-and-add resolution was 0″.6 FWHM. The data on Yale 9212 then served as a deconvolution key in a 500–1000 iteration Lucy-Richardson deconvolution (Lucy 1974) to CLEAN the wings of the point-spread function (the "seeing pedestal") from the NGC 7469 data. As a CLEAN-restoring beam for the deconvolved data, we used a Gaussian of FWHM 0″.4. Given the excellent signal-to-noise ratio (S/N) and large (factor of 10) oversampling of the point-spread function, this moderate "superresolution" can be achieved confidently, as shown by the excellent agreement of data sets taken at different times and wavelengths. Moreover, by using the Lucy-Richardson algorithm to reduce the input map to a series of delta functions which are subsequently reconvolved we avoid ringing, which is often present in maps of strictly deconvolved bright pointlike sources. Table 1 is a log of the SHARP observations.

2.2. *FAST Observations*

NGC 7469 was observed with the MPE 1–5 μm imaging spectrometer FAST (Rotaciuc 1992; Krabbe et al. 1993; Blietz 1994) in 1991 July/August on the 4.2 m WHT operated by the Royal Greenwich Observatory on La Palma, Canary Islands. FAST has a 58 × 62 pixel InSb array (pixel size 0″.5) placed behind a Fabry-Perot/circular-variable filter (FP/CVF) combination resulting in a velocity resolution of 330 km s^{-1} (FWHM) in the 1.95–2.4 μm (*K*) band. In the 1.5–1.8 μm (*H*) band only the CVF is used with a resolving power of ∼50. Table 2 gives a log of the different line observations of NGC 7469 carried out with FAST.

For the present analysis only that subset of all frames (integration times 50–200 s each in the different lines) that was obtained during the best seeing was selected, resulting in FWHM spatial resolutions given in Table 2. After subtraction of the dark current, the individual source and sky frames were flat-fielded and differenced and hot pixels and cosmic rays were interpolated. The resulting line-plus-continuum images were rebinned onto a grid of 0″.025 pixels and recentered on the continuum peak using a Gaussian fit to determine the shift

TABLE 1

LOG OF SHARP OBSERVATIONS ON THE NTT

Band	Date	$T_{\rm int}$(frame) (s)	*N*(frames)	$\Delta\theta_{\rm rg}$(FWHM)[a]	$\Delta\theta_{\rm Lucy}$(FWHM)[b]
J (1.25 μm)......	1993 Aug	2, 4	565	0″.6	0″.4
H (1.65 μm)......	1993 Aug	2	622	0.6	0.5
K (2.2 μm).......	1992 Aug	1, 2	3270	0.6	0.4

[a] "Raw" FWHM of star after recentering of rapid-guided frames.

[b] "Final" FWHM of point source after Lucy-cleaning and reconvolution.

TABLE 2

Log of FAST Observations on the WHT

Line	$\lambda_{\rm rest}$ (μm)	$(v - 4930)_{\rm obs}$ (km s^{-1})	$T_{\rm int}$[a] (minutes)	$\Delta v_{\rm res}$(FWHM) (km s^{-1})	$\Delta\theta_{\rm res}$(FWHM)
[Fe II] $^4D_{7/2}$–$^4F_{9/2}$......	1.6435	0	13	6000	1″.2
He I $n = 2\ ^1P$–^1S	2.0581	0	20	320	0.9
H_2 $v = 1$ S(1)...........	2.1212	0	38	320	0.9
H I n = 7–4 (Brγ)	2.1655	−40, +240	10	320	0.9

[a] Integration time per velocity channel.

vectors. Correction for atmospheric transmission and the instrumental profile was accomplished by dividing the line-plus-continuum images by a mean of the normalized spectra of the standard stars BS 8551 and HR 8781 (of spectral types K0 III and B9 V). Finally, the mean of the continuum on either side of the line was subtracted. The resulting pure-line images were co-added and flux calibrated with the above-mentioned standard star spectra. To remove artifacts in the continuum subtraction procedure arising from slight seeing variations, the images were low-pass filtered by applying a Lucy-Richardson deconvolution (Lucy 1974) followed by subsequent reconvolution to their original resolution. In the case of the 1.644 μm [Fe II] line, special care was taken to ensure accurate continuum subtraction since in low-resolution CVF mode the line-to-continuum ratio at the continuum peak is about a factor of 2–3 lower than in high-resolution FP mode (8% compared to 15%–20% in the *K* band). Subsequent data reduction steps then were identical to those for the He I, H_2, and Brγ data.

2.3. *IRSPEC Observations*

NGC 7469 was observed with the facility 1–5 μm long-slit, grating spectrometer IRSPEC (Moorwood, Moneti, & Gredel 1991) on the ESO NTT in 1992 June and 1994 May and September. The FWHM resolving power in the *K* band is ~2200 (velocity resolution 136 km s^{-1}). Spectra were taken in 1992 on the redshifted wavelengths of [Si VI] 1.9629 μm (Reconditi & Oliva 1993), H I n = 7–4 (Brγ) 2.1655 μm, and [Fe XII] 2.205 μm (Fuhr, Martin, & Wiese 1988). In 1994 we took additional observations of the $v = 0$–2 2.29 μm band of CO. A north-south oriented slit of width 4″.4 was used, and spectra presented here are integrated over four spatial pixels (8″.8) to include the complete nuclear region of NGC 7469. Total on-source integration times were 12 minutes for Brγ and [Fe XII], 36 minutes for [Si VI], and 22 minutes for CO. Data reduction followed standard procedures. For sky subtraction, individual integrations were obtained with NGC 7469 placed at different positions along the slit. Flux calibration and correction of atmospheric absorption features were achieved using spectra of the B9 V star HR 8781. The difference of ~20% in continuum level between the Brγ and [Fe XII] spectra is likely due to variable seeing and the fact that standard star observations were inserted between the observations at those wavelengths. The wavelength calibration of IRSPEC was checked against OH airglow lines from the list of Oliva & Origlia (1992). Corrections derived in this way and applied to the data never exceeded 50 km s^{-1}.

2.4. *3D Observations*

NGC 7469 was also observed with the new MPE field-imaging spectrograph, 3D, in its commissioning run (1993 December 1–7) on the 3.5 m telescope at Calar Alto, Spain. A detailed description of 3D is given in Weitzel (1994) and Weitzel et al. (1994). Briefly, 3D obtains $R = 1100$, 256-element *K*-band spectra simultaneously for every one of 16 × 16 pixels on the sky (0″.5 pixel^{-1} at Calar Alto). For this purpose, an image slicer rearranges the two-dimensional focal plane along the long slit of an $R = 1100$ grism. The dispersed spectra are then collected on a 256 × 256, HgCdTe NICMOS3 detector array. The multiplexed three-dimensional data cube (two spatial and one spectral dimension) is then reassembled post facto during the data reduction. Seeing during these observations was near 1″ resulting in FWHM 1″.1 × 0″.9 (east-west × north-south) in the *K* band. The observations consisted of 100 s on-nucleus, 100 s off-nucleus (60″ south) pairs. A total of 3900 s of on-source integration time was acquired in three nights. Spatial flat-fielding was achieved using a dome exposure, and spectral flat-fielding was done with a Nernst glower, tuned to $T = 1300$ K. The emission lines of a neon discharge lamp served as a spectral calibration source. The star HR 8781 (B9 V) served for correction of the absorption of the Earth's atmosphere where the stellar Brγ absorption line was removed by interpolation. As the detector pixels are spaced by one spectral resolution element ($\Delta\lambda/\lambda = 10^{-3}$), the spectra are undersampled.

The data reduction was carried out with the GIPSY package developed at the University of Groningen. In order to account for the special structure and quality of the 3D data frames, a substantial number of algorithms and subroutines were written and added to the available procedures. The images were corrected for nonlinear detector response, then background subtracted and divided by the flat field. The spectral calibration included a rebinning of the data frames onto a linear wavelength grid. The pixels in each frame were rearranged onto a 16 × 16 × 300 pixel data cube, with the first two coordinates corresponding to the spatial and the third corresponding to the spectral information. Bad pixels and cosmic-ray hits could be corrected by interpolation in most cases if enough good data pixels in the three-dimensional neighborhood were available. Before co-adding the data cubes, individual frames were rebinned onto a 0″.25 grid and recentered on the continuum peak. Parallel to the data cubes, so-called mask cubes were constructed containing information about residual bad pixels, the relative positions of the frames after recentering, and their relative statistical weight (proportional to the square root of integration time). The final weighted mosaic cube of the object was computed from ~60 data/mask cubes. Finally, the result was divided by the normalized standard star spectrum and spatially smoothed to the original resolution.

A pseudo–*K*-band image was computed by collapsing the high-S/N images in the cube. The line maps were constructed by adding up the relevant on-line channel maps and subtracting a number of appropriate continuum channel maps in the vicinity of the line normalized to the number of on-line channels.

3. RESULTS

This section contains a discussion of the basic results of our infrared observations, along with comparisons to relevant measurements at other wavelengths. More detailed analysis and theoretical interpretations can be found in §§ 4 and 5.

Figures 1–4 present the near-infrared maps and spectra, and Table 3 lists the derived line fluxes and continuum flux densities. Figure 1 (Plate 9) shows the 0″.4 *J*- and *K*-band SHARP Lucy-cleaned maps and a 0″.6 $J-K$ color map. The *H*-band map (not shown) is similar to the *J*- and *K*-band maps but of somewhat poorer quality. Figure 2 (Plate 10) gives the 3D spectrum of the central 2″.5 and the $\approx 1''$ (FWHM) 3D-maps of [Si VI], He I, Brγ, and H_2 *S*(1) (all integrated over the specified velocity ranges and continuum subtracted) and CO $v = 0$–2 absorption optical depth, along with a corresponding broad-band 2.2 μm continuum map. Figure 3 displays IRSPEC spectra of the central 4″.4 × 8″.8. Figure 4 shows the $\leq 1''$ (FWHM) resolution [Fe II], He I, Brγ, and H_2 *S*(1) FAST line maps (continuum subtracted and integrated over the observed velocity channels), along with a narrowband map of the 2.2 μm continuum for comparison. In addition, Figure 5 (Plate 11) shows comparisons of our high-resolution near-infrared maps to maps at other wavelengths.

Comparisons of spectra of the same wavelength regions taken with both IRSPEC and 3D ([Si VI] + H_2 *S*(3), Brγ, and Na I; Figs. 2 and 3) and maps common to FAST and 3D (H_2 *S*(1), Brγ, and He I; Figs. 2 and 4) show good agreement even in detail. Similarly, the high-resolution SHARP *J*- and *K*-band maps compare very well with the 5430, 6130, and 6660 Å speckle maps of Mauder et al. (1994), and with the 0″.65 Lucy-restored *K*-band map of Mazzarella et al. (1994). Integrated line fluxes of IRSPEC, FAST, and 3D also typically agree to within ±30%, but greater differences can occur when trying to separate contributions from ring and nucleus with different beam sizes. Our fluxes are significantly larger (factor of ≈ 2) than those of Moorwood & Oliva (1988). The reason for this discrepancy is not clear. We now describe our results in detail.

3.1. *Nucleus and Ring*

The near-infrared continuum maps and the Brγ and $v = 0$–2 CO line maps show clear evidence for two main components of emission, the unresolved (intrinsic FWHM < 0″.3 or 100 pc), bright Seyfert nucleus, as well as an extended, circumnuclear emission region (diameter $\geq 4''$), in agreement with the results in the optical, mid-infrared, and radio tracers mentioned in the Introduction (Wilson et al. 1991; Mazzarella et al. 1994;

TABLE 3

OBSERVED NEAR-INFRARED FLUX DENSITIES AND FLUXES IN NGC 7469[a]

A. FLUX DENSITIES

BAND	FLUX DENSITY (mJy) Nucleus[b]	Ring[c]	BEAM	COMMENTS
J (1.25 μm)	17.5 ± 2	22.5 ± 3	0″.4	SHARP, M94[d]: 20 mJy (N), 26 mJy (R)
H (1.65 μm)	35 ± 6	36 ± 6	0.5	SHARP, M94[d]: 36 mJy (N), 37 mJy (R)
K (2.2 μm)	60 ± 6	35 ± 4	0.4	SHARP, M94[d]: 61 mJy (N), 40 mJy (R)

B. FLUXES

LINE	FLUX (ergs s^{-1} cm^{-2}) Nucleus[b]	Ring[c]	BEAM	COMMENTS
[Fe II] 1.644 μm	4.8×10^{-14}	$\leq 4 \times 10^{-14}$(2 σ)	1″.2	FAST, M88[d]: 3.1×10^{-14} (6″ × 6″)
H_2 *S*(3) 1.957 μm	2.3×10^{-14}		4.4 × 8.8	IRSPEC, $v_{\rm hel} = 4940 \pm 70$ km s^{-1}[e]
[Si VI] 1.963 μm	2.8×10^{-14}		4.4 × 8.8	IRSPEC
[Si VI] + H_2 *S*(3)	4×10^{-14}	$\leq 1 \times 10^{-14}$	1.0	3D, [Si VI] (N) $\approx 3.2 \times 10^{-14}$, $v_{\rm hel} = 4430 \pm 150$ km s^{-1}[e]
He I 2.058 μm	7.4×10^{-15}	7×10^{-15}	0.9	FAST
He I 2.058 μm	$\approx 10^{-14}$	...	1.0	3D
H_2 *S*(1) 2.121 μm	7×10^{-15}	1.4×10^{-14}	0.9	FAST, M88[d]: 1.1×10^{-14} (6″ × 6″)
H_2 *S*(1) 2.121 μm	1.2×10^{-14}	1.2×10^{-14}	1.0	3D, H86[d]: 1.7×10^{-14} (4″.5)
H I Brγ 2.166 μm (narrow component)	3.0×10^{-14}		4.4 × 8.8	IRSPEC, M88[d]: 1.2×10^{-14} (6″ × 6″)
	1.2×10^{-14}	2.5×10^{-14}	0.9	FAST, $v_{\rm hel}$(IRSPEC, FAST) $= 4920 \pm 70$ km s^{-1}[e]
	1×10^{-14}	2×10^{-14}	1.0	3D
	[$\Delta v_{\rm intr}$(FWHM) = 200 km s^{-1}]			
H I Brγ 2.166 μm (broad component)	$\geq 1.5 \times 10^{-14}$		4.4 × 8.8	IRSPEC
	3×10^{-14}		1.0	3D, $v_{\rm hel} = 4500 \pm 200$ km s^{-1}[e]
	[$\Delta v_{\rm intr}$(FWHM) $\geq$ 1200 km s^{-1}]			
[Fe XII] 2.205 μm	$\leq 3 \times 10^{-15}$ (2 σ)		4.4 × 8.8	IRSPEC
Na I 2.207 μm	EW $\approx$ 1.2 Å[f]		4.4 × 8.8	IRSPEC
CO 2.29 μm $v = 0$–2 spectroscopic index[g]	≤ 0.05	0.16 ± 0.02	1.0	3D
	...	0.17 ± 0.02	4.4 × 8.8	IRSPEC

[a] Line fluxes are integrated over the observed velocity channels and are given in ergs s^{-1} cm^{-2}, continuum flux densities in millijanskys, uncertainties typically ±30%.

[b] Within a radius $\leq$0″.7.

[c] Integrated between 0″.7 and 2″.5 in radius from nucleus.

[d] M88 = Moorwood & Oliva 1988; M94 = Mazzarella et al. 1994; H86 = Heckman et al. 1986; R94 = Ridgway & Wynn-Williams 1994; (N) stands for nucleus, (R) for ring.

[e] Heliocentric velocity of line centroid.

[f] Equivalent width.

[g] Spectroscopic index of $v = 0$–2 band defined as [line(2.25 μm) − continuum(< 2.27 μm)]/continuum(2.25 μm).

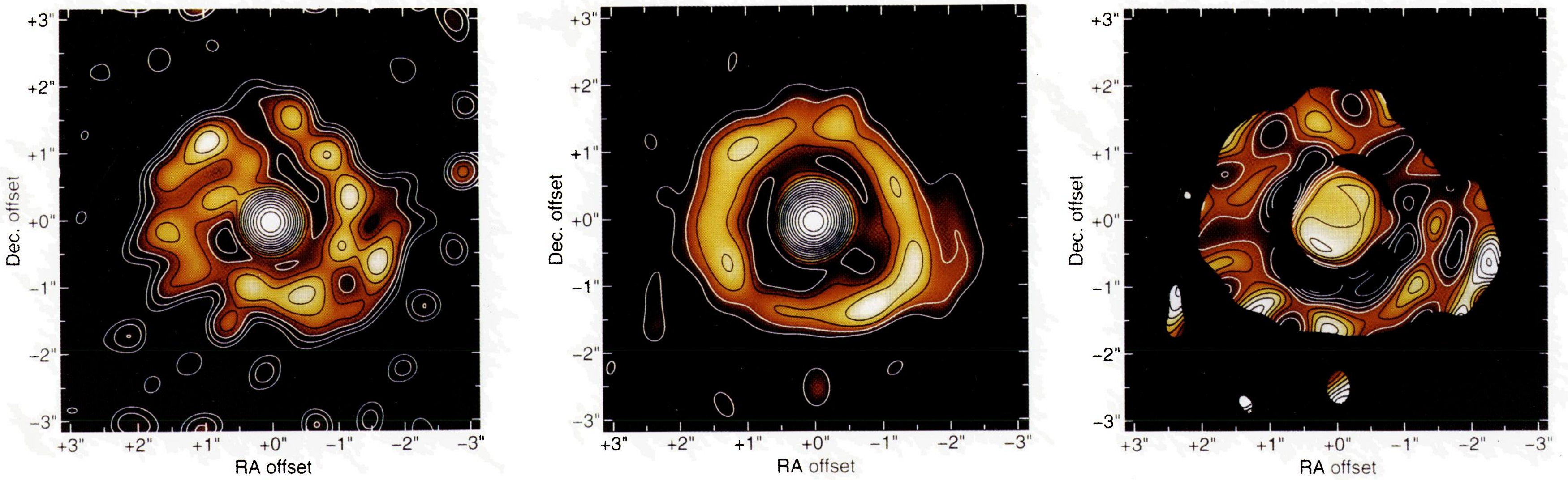

FIG. 1.—Contour maps/color images of SHARP images of NGC 7469. *Left*: $0\farcs4$ FWHM *J*-band image. Contours are 0.8, 1.1, 1.6, 2.2, 3.1, 4.4, 6.3, 8.8, 12.5, 17.7, 25, 35, 50, 71, and 100 percent of 0.19 mJy/$(0\farcs05)^2$. *Middle*: $0\farcs4$ *K*-band image. Contours are 0.55, 0.78, 1.1, 1.6, 2.2, 3.1, 4.4, 6.3, 8.8, 12.5, 17.7, 25, 35, 50, 71, and 100 percent of 0.65 mJy/$(0\farcs05)^2$. *Right*: $J-K$ color map. Contours are $J-K = 0.4, 0.7, 1, 1.3, 1.6, 1.9, 2.2, 2.5, 2.8, 3.1, 3.4$, and 3.7 mag. See text and Table 1 for details.

GENZEL et al. (see 444, 132)

1995ApJ...444..129G

NGC 7469

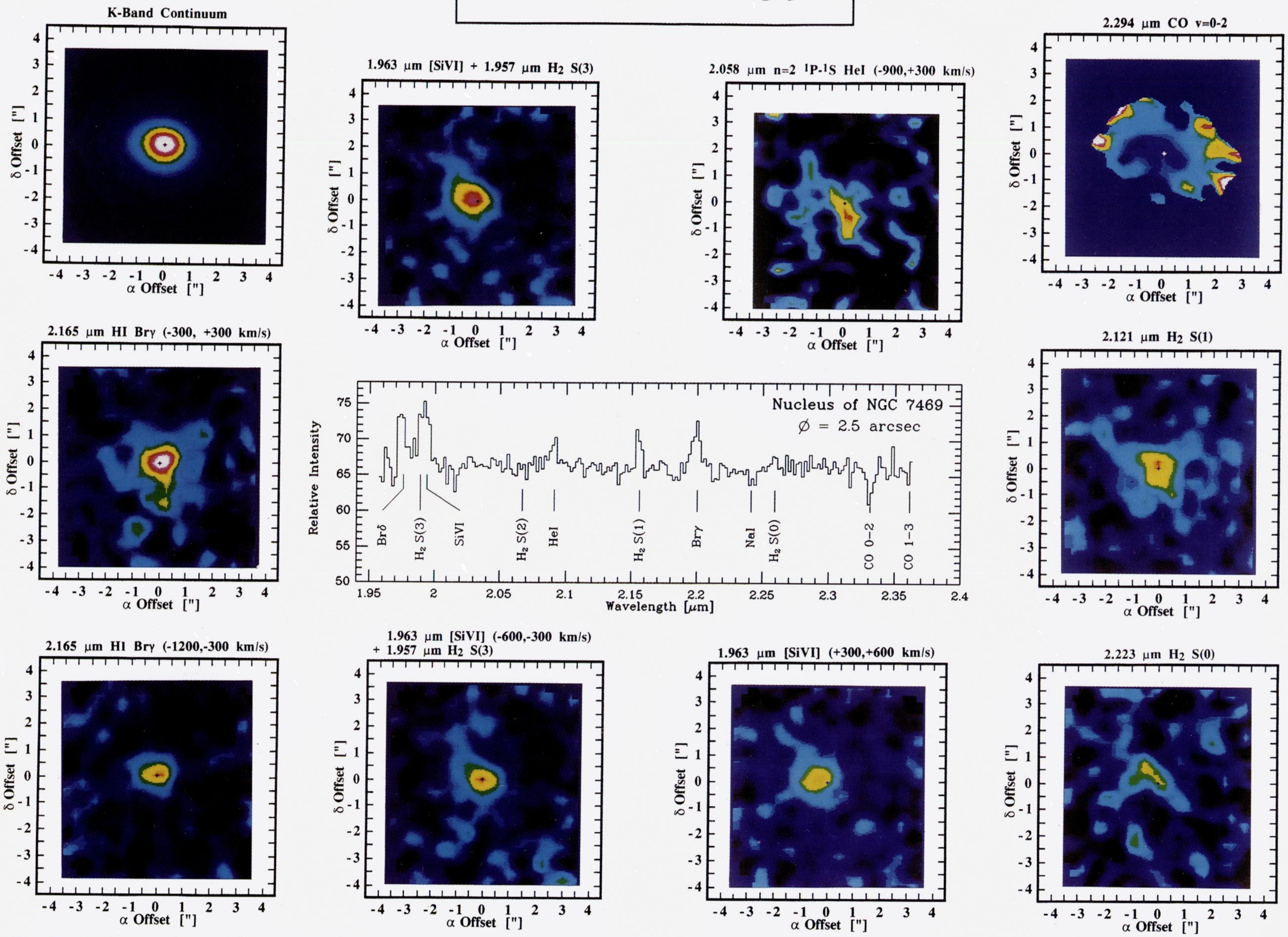

FIG. 2.—Continuum-subtracted 3D spectrum of the nucleus (central 2″.5; *center*) and color images of the flux distributions of individual lines (and velocity ranges, if given), along which a pseudo–*K*-band continuum image. In the case of the CO $v = 0$–2 absorption band map, the spectroscopic index is plotted (see text and Table 3), with a mask cutting off the regions with no significant continuum flux at $R \geq 2''.5$. The large values of the CO index at the edges of the map are due to poor S/N, and the CO index in the circumnuclear ring is about constant (≈ 0.16) with the exception of the peak southwest of the nucleus. Spectral resolution is 270 km s^{-1} with a sample every 300 km s^{-1}. Spatial resolution is 1″ FWHM. The color scale of the images is linear in flux. The continuum peak is marked on all images as a small cross.

GENZEL et al. (see 444, 132)

1995ApJ...444..129G

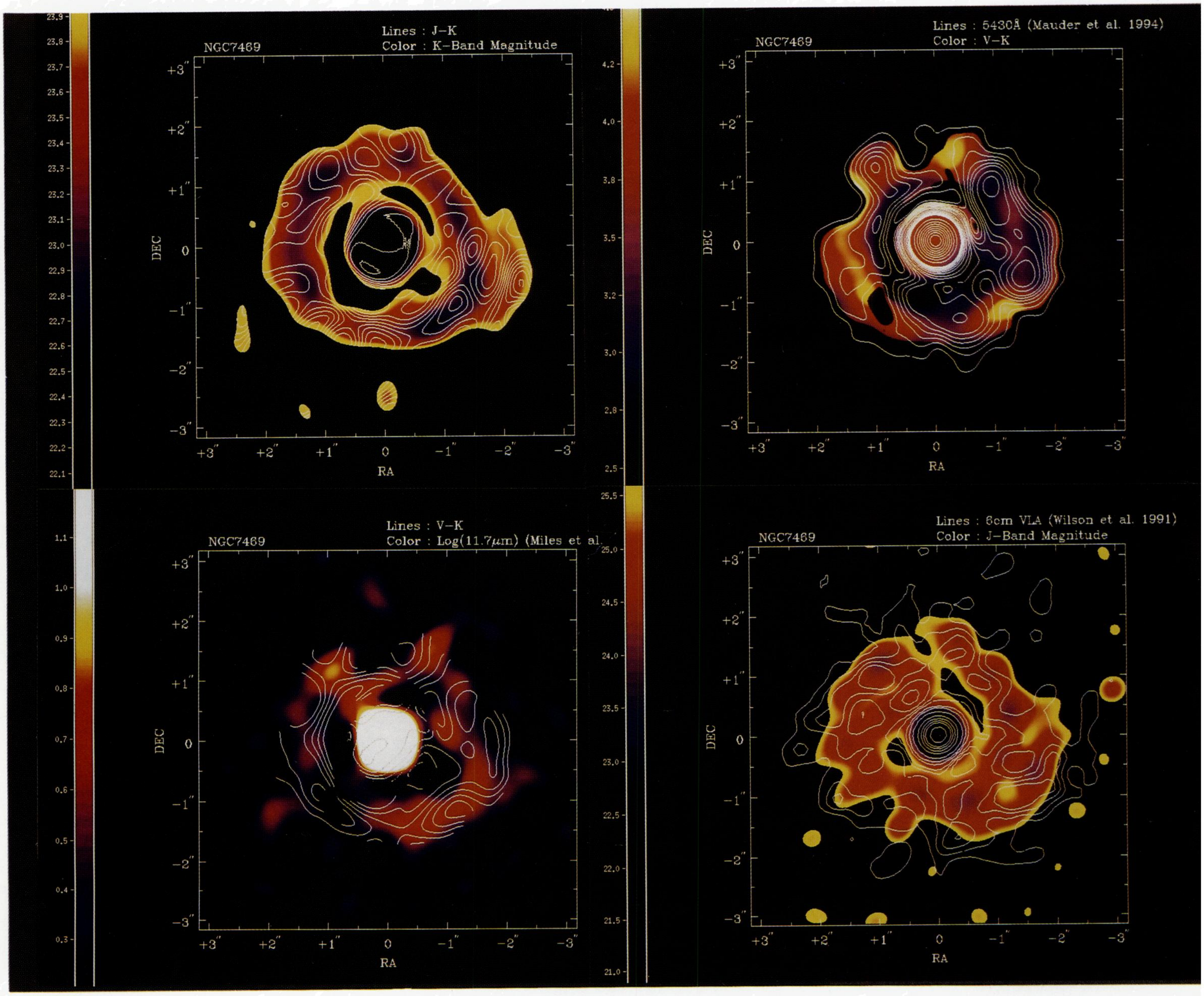

FIG. 5.—Comparison of different data sets. *Top left*: Contours of 0″.6 (FWHM) $J-K$ color map overlayed on K-band SHARP image (false color, 0″.4; color scale is shown on the left in magnitudes per 0″.05 pixel). The contours are $J-K = 0.4, 0.7, \ldots, 3.7$. *Top right*: Contours of 5400 Å narrowband continuum (0″.3; Mauder et al. 1994) overlayed on top of 5400 Å ($\approx V$) $- K$ color (false color, 0″.4; color scale shown on the left). The contours are 0.75, 1, 1.25, 1.5, 1.75, 2, 2.5, 3, and 4, …, 10, 20, 30, …, 90 percent of 4 μm Jy per $(0''.011)^2$ pixel. *Bottom left*: 5400 Å $- K$ color (contours) on top of 11.7 μm dust continuum (false color, 0″.6; Miles et al. 1994; log [$S(11.7)$ in mJy arcsec^{-2}] scale shown on left). The contours are $V-K = 2.5, 2.8, \ldots, 4.3$. *Bottom right*: 5 GHz radio continuum (contours, 0″.38; Wilson et al. 1991) overlayed on top of J-band SHARP image (false color, 0″.4; color scale in magnitudes per 0″.05 pixel is shown on left). The contours are 1.5, 2, 2.5, 3, 4.5, 6, 10, 20, …, 50, 75, and 100 percent of 18 mJy per 0″.39 × 0″.37 (FWHM) beam area.

GENZEL et al. (see 444, 132)

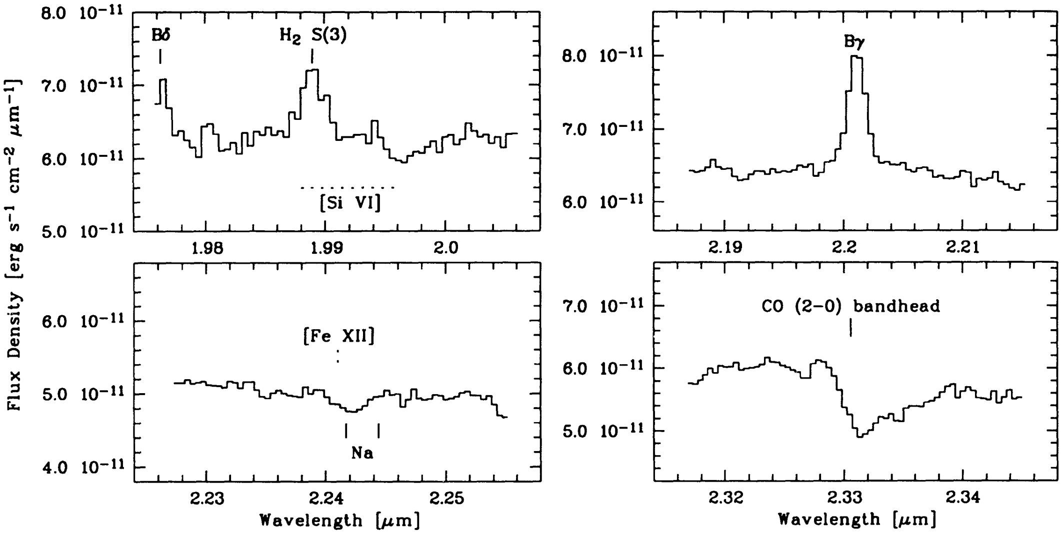

FIG. 3.—IRSPEC spectra of H_2 $S(3)$/[Si VI] (*top left*), H I $n = 7$–4 (Brγ) (*top right*), Na I/[Fe XII] (*bottom left*), and CO $v = 0$–2 (*bottom right*). Spectral resolution is 136 km s^{-1}, spatial resolution 4".4 × 8".8.

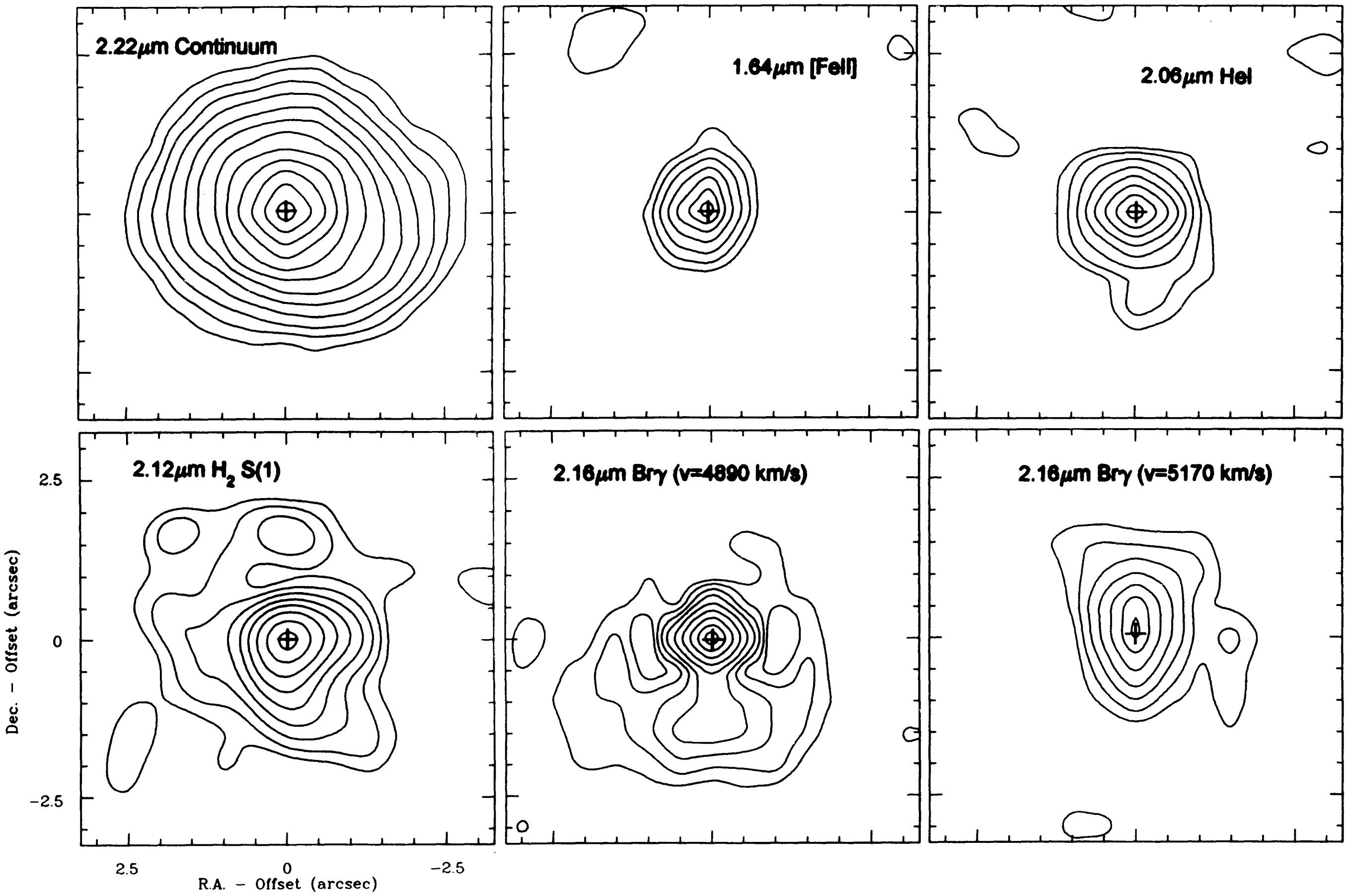

FIG. 4.—FAST narrowband maps of the nucleus of NGC 7469. On all line maps the continuum has been subtracted. The Seyfert nucleus is at (0, 0) (*cross*). *Top left*: 0".9 (FWHM) map of 2.22 μm CVF continuum. Contour levels are 3, 4, 5, 9, 11, 15, 23, 37, 54, 74, and 93 percent of 1.3 ergs cm^{-2} s^{-1} sr^{-1} μm^{-1}. *Top center*: 0".9 map of 1.64 μm [Fe II], taken with the CVF at resolving power $R = 50$. Contour levels are 11, 23, 38, 55, 72, 86, and 96 percent of 2.7×10^{-3} ergs cm^{-2} s^{-1} sr^{-1}. *Top right*: 0".9 map of 2.06 μm $n = 2$ ^1P–^1S He I at 330 km s^{-1} resolution centered on 4930 km s^{-1}. Contour levels are 11, 14, 22, 33, 45, 59, 76, and 94 percent of 6.7×10^{-4} ergs cm^{-2} s^{-1} sr^{-1}. *Bottom left*: 1".0 map of 2.12 μm H_2 $v = 1$–0 $S(1)$ at 330 km s^{-1} resolution centered on 4930 km s^{-1}. Contour levels are 7, 9, 13, 18, 27, 37, 53, 74, and 95 percent of 8×10^{-5} ergs cm^{-2} s^{-1} sr^{-1}. *Bottom center*: 0".9 map of 2.16 μm H I $n = 7$–4 (Brγ) at 330 km s^{-1} resolution, centered on $v_{\rm hel} = 4890$ km s^{-1}. Contour levels are 8, 11, 16, 22, 30, 43, 59, 77, and 94 percent of 1.2×10^{-3} ergs cm^{-2} s^{-1} sr^{-1}. *Bottom right*: 0".9 map of 2.16 μm Brγ at 330 km s^{-1} resolution, centered on 5170 km s^{-1}. Contour levels are 20, 28, 38, 50, 66, 84, and 98 percent of 2.4×10^{-4} ergs cm^{-2} s^{-1} sr^{-1}.

Mauder et al. 1994; Miles et al. 1994). The SHARP maps in Figure 1 show that the brightest part of the near-infrared circumnuclear emission comes from a nearly circular, clumpy ring at a radius of ~1″.5 (480 pc) from the bright Seyfert nucleus. We note here that we have done extensive tests with artificial data sets to show that the ring structure could not have been created as an artifact of improper cleaning (see also § 2.4). The SHARP maps leave open for discussion/interpretation whether the ring is complete, or whether it actually consists of two tightly wound, counterclockwise spiral arms east and west of the nucleus, as favored by Mazzarella et al. (1994). While the surface brightness of the circumnuclear ring is much lower than that of the nucleus (e.g., a factor of ≤ 50 in the 0″.4 SHARP data), both components contribute about the same fraction of the total flux in the various tracers (Table 3 and Fig. 7). Clearly the circumnuclear region contributes a substantial fraction to the total energy budget of the central 10″. The 2.3 μm CO bandhead absorption feature also peaks in the ring (Fig. 2). The mean spectroscopic $v = 0$–2 bandhead depth, defined as the ratio of the peak absorption depth at 2.33 μm to the continuum at ≤ 2.3 μm, is 0.16 ± 0.02 (Figs. 2 and 3; Ridgway & Wynn-Williams 1994). For a stellar 2.3 μm continuum made up entirely of late-type giants and supergiants, for a ring velocity dispersion of ≈ 110 km s^{-1} (see below) and spectral resolving power of 3D, the bandhead depth would be ~0.2, not much larger than the observed depth. The absorption feature at 2.242 μm (Figs. 2 and 3) due to Na I is also likely stellar, and the ratio of its equivalent width relative to that of CO (≈ 0.3) is approximately consistent with that found in late-type stars (e.g., Kleinmann & Hall 1986). Thus, most of the K-band flux in the ring is stellar. Hα and [O III] spectroscopy (DeRobertis & Pogge 1986; Wilson et al. 1986) demonstrates that the ring is rotating about the nucleus with an observed velocity of ~100 km s^{-1}. The position angle of the major axis for the gas $R \geq 3''$ is ~135° (DeRobertis & Pogge 1986; Wilson et al. 1986).

3.2. *Blueshifted Ridge South of the Nucleus*

In addition to nucleus and ring, the FAST and 3D maps of Brγ, He I, and perhaps H_2 $S(1)$ show a 1″ ridge of emission emanating from the nucleus to the south (Figs. 2 and 4). This ridge is blueshifted (≥ 50 km s^{-1} in Brγ; Fig. 4) and extends from the nucleus to 1″.5 south, at about the radius of the circumnuclear ring. Wilson et al. (1986) and DeRobertis & Pogge (1986) have previously found high-excitation ([O III]/H$\beta > 1$) gas south and east of the nucleus, near the region of the ridge, that is also blueshifted (by 50–150 km s^{-1}) and does not participate in the rotation of the ring. The ridge is present in the radio continuum map of Wilson et al. (1991) as well, with perhaps some evidence for a corresponding counterridge north of the nucleus. The radio emission in the circumnuclear ring may bend inward at the location of the blueshifted ridge, suggesting either that ridge and ring are interacting there, or perhaps that the ridge is a material arm connecting the ring/spiral-arm system with the nucleus. The 6660 Å (Hα/[N II] + continuum) and 5430 Å ([O III] + continuum) maps of Mauder et al. (1994, Fig. 5) also show emission between the nucleus and southern part of the ring. As both maps contain line emission as well as continuum emission, it is not obvious whether this emission is nebular or stellar. We estimate from the line fluxes of Bonatto & Pastoriza (1990) that line emission contributes between 25% and 50% to the 6660 Å map and between 7% and 15% to the 5430 Å map. We conclude that the ridge is a third, kinematically distinct component, either caused by gas flowing out of the nucleus (i.e., a classical extended narrow-line region [NLR] or outflow cone), or by gas streaming radially inward (along a material arm or bar) from ring to nucleus. Higher resolution imaging spectroscopy is required to resolve this ambiguity. The high excitation of the ridge gas, as indicated by the presence of strong He I and [O III] emission, suggests that the gas is photoionized by a hard UV continuum, probably located in the nucleus (Wilson et al. 1986).

3.3. *Emission Knots and Evidence for Intrinsic Extinction*

The circumnuclear ring contains compact ($\leq 0''.4$ or ≤ 130 pc) continuum emission knots (Fig. 1; Mauder et al. 1994). The overall near-infrared morphology, including the approximate locations of the brightest knots, is similar to that found in the visible, in the mid-infrared, and in the radio continua, all taken at comparable spatial resolutions. This is demonstrated in Figure 5 which shows comparisons of the SHARP K-band and $J-K$ color maps to the 5400 Å ($\approx V$ band + [O III]) map of Mauder et al. (1994), the 11.7 μm map of Miles et al. (1994), and the 5 GHz VLA radio map of Wilson et al. (1991).

Despite this good overall agreement of all data sets there are significant differences in detail. In particular, the shorter wavelength distributions (J, R, and V) appear to be spottier than the relatively smooth K-band map. This is most likely a signature of extinction by dust mixed in with the stars (cf. Sams et al. 1994). While the optical and near-infrared maps are roughly aximuthally symmetric, the radio and 11.7 μm maps are more asymmetric. The strongest radio and 11.7 μm dust emission originates from the portions of the ring northeast and southwest of the nucleus. The radio/mid-infrared emission peaks appear to be significantly (0″.4–0″.5) offset from the corresponding $V/R/J$ peaks, and the prominent $V/R/J$ ridge northwest of the nucleus has little corresponding radio/mid-infrared emission. Again, this anticorrelation is likely a signature of extinction by embedded dust. In fact, the locations of reddest $J-K$ and $V-K$ colors (tracing mainly extinction) are reasonably well correlated with the peaks of dust and nonthermal radio continuum emission (Fig. 5), as expected in such a scenario.

We conclude that dust clouds embedded in the stellar distribution locally affect the visible and near-infrared emission distribution. The northeast and southwest portions of the ring, located on opposite sides of the nucleus, correspond to local density concentrations of interstellar gas and dust. The nonthermal radio emission (presumably from supernova remnants; Wilson et al. 1991) is stronger there either because it does not suffer from extinction, or because the larger density of interstellar gas causes an increase in its brightness. The zone between 0″.8 and 1″.2 radius from the nucleus has the bluest colors, and the Miles et al. 11.7 μm map also shows less dust there. This suggests that there is a gap in the gas density at $R \approx 300$ pc, although detailed conclusions are not possible because of the difficulty in reliably estimating and removing the wings of the bright central source so close to it.

The fact that the near-infrared emission is significantly affected by spatially variable extinction immediately indicates that the extinction involved must be relatively large ($A_K \geq 1$ or $A_V \geq 10$). This assessment is consistent with the large column density of gas implied by the millimeter CO 1–0 observations of Meixner et al. (1990). Applying the Galactic $N(H_2)/I(\mathrm{CO})$ conversion factor X_G ($X_G = 2.3 \times 10^{20}$ cm^{-2} (K km s^{-1})$^{-1}$;

Strong et al. 1988) to their observed CO flux in the central 5″ (200 Jy km s^{-1} or 740 K km s^{-1}) results in an average H_2 column density of 1.7×10^{23} cm^{-2}, or $A_V \approx 160$ (see, however, § 4.3 for evidence that the conversion factor is ∼5 times smaller than X_G). We will show below (§ 4.1) that the observed optical/infrared colors and hydrogen recombination line ratios can also be quantitatively accounted for by such a model of embedded dust extinction.

We find that even after correction for this intrinsic dust extinction the ring still contains emission knots which we interpret as *supergiant star formation complexes.* These "superclouds" must be conglomerates of very massive molecular clouds ($\geq 10^8$ $M_\odot$), OB associations, red/blue supergiants, and supernova remnants, probably similar to scaled-up versions of the Large Magellanic Cloud (LMC) 30 Dor region (Walborn 1991), and comparable to the giant extragalactic H II regions and young globular clusters recently found with the *Hubble Space Telescope* (Holtzmann et al. 1992; Conti & Vacca 1994).

3.4. *Coronal Gas*

The nuclear spectrum derived from the 3D data set (Fig. 2) shows a broad (FWHM 1400 km s^{-1}, full-width at zero power [FWZP] > 2500 km s^{-1}) emission line centered at 1.992 ± 0.001 μm. The 1.99 μm emission region is compact (intrinsic diameter ≤1″, or ≤160 pc in radius) and centered on the 2 μm continuum peak. Its spectral shape is similar to that of Brγ and much broader than that of H_2 S(1). We identify this line with $^2P_{1/2}$–$^2P_{3/2}$ [Si VI] (rest wavelength 1.9629 μm; Reconditi & Oliva 1993), with a contribution from 1.957 μm H_2 S(3). Given the strength of H_2 S(1) in the central 1″ (Fig. 2), the lack of H_2 S(2) at 2.04 μm, and the typical H_2 S(3)/S(1) intrinsic ratios observed in other sources and expected theoretically [$S(3)/S(1) \leq 1$; e.g., Sternberg & Dalgarno 1989], H_2 S(3) probably contributes no more than 40% to the 1.992 μm line in the central 1″.5. This changes with aperture, as the [Si VI] emission is compact while the H_2 S(3) emission is spatially extended. The IRSPEC 4″.4 × 8″.8 spectrum at 1.99 μm (Fig. 3) shows a strong, narrow H_2 S(3) line superposed on a broad feature whose centroid, width, and flux are approximately consistent with the 3D 1.992 μm feature in the central 1″.5 (Table 3). If a spectrum of the circumnuclear region excluding the nucleus is created from the 3D data cube, the line centroid is at 1.990 μm, consistent with H_2 S(3) contributing strongly, as in the IRSPEC spectrum. Shortward of [Si VI] + H_2 S(3) is Brδ at 1.98 μm, approximately in the expected ratio relative to Brγ (≈0.6) (Figs. 2 and 3). Figure 2 shows that the blueshifted and redshifted parts of the emission are shifted with respect to each other by ≈0″.3 east-west. While this finding needs to be confirmed, it may indicate that we are on the verge of spatially resolving the [Si VI] emission.

The observed nuclear line centroid (1.992 ± 0.001 μm) then suggests that the [Si VI] line is blueshifted by 300–450 km s^{-1} [depending on the effect of 1.989 μm H_2 S(3)]. In a study of [Fe X]/[Fe XI] coronal lines in the visible waveband, Penston et al. (1984) found that these coronal lines are almost always blueshifted with respect to [O I] 6300 Å (average blueshift 120 km s^{-1}). In a sample of about a dozen active galaxies, NGC 7469 showed the largest such blueshift. The 6374 Å [Fe X] line in NGC 7469 is at $v_{\rm hel} = 4470$ km s^{-1}, or blueshifted by 460 km s^{-1} with respect to the systemic velocity of 4930 km s^{-1} (Penston et al. 1984), consistent with our [Si VI] result. In three other galaxies where both 1.96 μm [Si VI] as well as coronal lines in the visible have been observed (NGC 1068, Circinus, and IC 4329A), the (blueshifted) velocities of infrared and visible coronal lines agree as well (Oliva & Moorwood 1990; Oliva et al. 1994). The intrinsic width of the [Si VI] line in NGC 7469 (1100–1300 km s^{-1} FWHM) is significantly larger than that of the [Fe X] line (650 km s^{-1}), again in agreement with the findings in NGC 1068 and IC 4329A.

Correcting the observed 3D flux for H_2 S(3) results in an [Si VI] flux of $\approx 3.2 \times 10^{-14}$ ergs s^{-1} cm^{-2} (Table 3). The [Si VI] luminosity is $\sim 4.5 \times 10^6$ $L_\odot$, or $\sim 3 \times 10^{-5}$ of the bolometric luminosity of the nucleus ($\approx 1.5 \times 10^{11}$ $L_\odot$; see § 4.2). Similarly, Oliva & Moorwood (1990) find that the 1.96 μm [Si VI] line toward the nucleus of NGC 1068 has a line luminosity of 5×10^6 $L_\odot$, again 3×10^{-5} of its bolometric luminosity (1.5×10^{11} $L_\odot$). The line width of the [Si VI] line in NGC 1068 (1100 km s^{-1}) is also quite similar to the value we find in NGC 7469. We conclude that the coronal gas in both galaxies is located inside the NLR, and probably between the broad-line region (BLR) and the NLR. We come back to the physical conditions of the coronal gas in § 5.2.

3.5. *Partially Ionized Gas*

Intense near-infrared [Fe II] line emission (especially relative to Brγ) in galactic nuclei can be plausibly interpreted in terms of fast shocks or X-ray excitation, as the result of the interaction of fast winds/jets or expanding supernova shells with surrounding dense clouds (Moorwood & Oliva 1988; Greenhouse et al. 1991; van der Werf et al. 1993; Blietz et al. 1994). NGC 7469 fits into this scenario as well. The [Fe II]/Brγ (narrow) line flux ratio (≥3 in the nucleus and ≤2 in the ring) is similar to that found in other infrared luminous galaxies (e.g., Forbes & Ward 1993) and clearly much larger than in normal H II regions with standard (i.e., depleted) iron abundance. As discussed in Blietz et al. (1994), both shock excitation (e.g., in supernova remnants) and X-ray excitation can explain such [Fe II]/Bγ ratios. Furthermore, the ratio of [Fe II] flux to 5 GHz flux density in NGC 7469 (2.3×10^{-15} ergs s^{-1} cm^{-2} mJy^{-1} in the nucleus and $\leq 4 \times 10^{-15}$ in the ring) is also quite consistent with the average ratio [$(2.5 \pm 1) \times 10^{-15}$] found by Forbes & Ward (1993) for other starburst and Seyfert galaxies.

3.6. *Hot Molecular Gas*

The FAST and 3D maps in Figures 2 and 4 show that there is a substantial concentration of hot ($T \geq 10^3$ K) molecular gas in the nucleus of NGC 7469, in addition to the extended component associated with the ring and southern ridge. About one-third to half of the total line flux (Table 3) originates from within a few tenths of an arcsecond (≈100 pc) of the nucleus. Assuming that the vibrationally excited H_2 line emission traces the overall distribution of all the molecular hydrogen gas (cold as well as hot), as is the case in the nucleus of NGC 1068 (Tacconi et al. 1994), the H_2 data thus suggest that molecular gas is concentrated within the central NLR of NGC 7469, similar to the finding for the Seyfert 2 galaxy NGC 1068 (Rotaciuc et al. 1991; Blietz et al. 1994; Tacconi et al. 1994).

4. STARBURST MODELS OF THE CIRCUMNUCLEAR RING

In this section we show that the various optical, infrared, and radio observations of the circumnuclear ring can be quantitatively accounted for by a powerful starburst and discuss its derived properties. We begin with a discussion of the key input parameters.

4.1. *Extinction Correction*

To derive extinction corrections for the visible and near-infrared data points we adopted the Draine (1989) extinction curve [$A(\mathrm{H}\beta) = 1.1A_V$, $A(\mathrm{H}\alpha) = 0.8A_V$, $A(R) = 0.72A_V$, $A(J) = 0.28A_V$, $A(H) = 0.16A_V$, and $A(K) = A(\mathrm{Br}\gamma) = 0.11A_V$]. From the H$\beta$/Br$\gamma$ ratio in the ring (Tables 3 and 4) and case B recombination theory ($n_e = 10^4$ cm^{-3}, $T_e = 8000$ K, and $I(\mathrm{H}\beta)/I(\mathrm{Br}\gamma) = 34$; Osterbrock 1989) we derive a visual extinction of 2.1 ± 0.3 [$A(\mathrm{H}\beta) - A(\mathrm{Br}\gamma) = E(\mathrm{H}\beta - \mathrm{Br}\gamma) = 2.1$]. Here we have assumed a simple foreground screen geometry for the absorbing dust so that the observed source intensity at frequency ν depends exponentially on dust optical depth ($I(\nu) \propto \exp[-\tau_{\mathrm{dust}}(\nu)]$). Similarly, for the observed Hα/Hβ ratios in the narrow-line gas (Wilson et al. 1986, 1991; Heckman et al. 1986; Bonatto & Pastoriza 1990) we infer a screen visual extinction between 2 and 3 [$E(\mathrm{H}\beta - \mathrm{H}\alpha) = 0.6$–$0.9$]. The extinction can also be estimated from the broadband visual/near-infrared colors of the ring. The intrinsic colors of $t \geq 10^7$ yr starbursts from the star cluster model described below are $(V-K)_{\mathrm{SB}} = 1.6 \pm 0.2$, $(R-K)_{\mathrm{SB}} = 1.3 \pm 0.2$, $(J-H)_{\mathrm{SB}} = 0.3 \pm 0.1$, and $(J-K)_{\mathrm{SB}} = 0.5 \pm 0.1$ (see also Mas-Hesse & Kunth 1991). With these intrinsic colors and the observed $V-K$, $R-K$, $J-H$, and $J-K$ colors of the ring ($V-K = 3.75$, $R-K = 3.0$, $J-H = 1.0$, and $J-K = 1.45$), we find $A_V = 2.4 \pm 0.2$ [$E(V-K) = 2.15$], $A_V = 2.8 \pm 0.3$ [$E(R-K) = 1.7$], $A_V = 5.8 \pm 0.5$ [$E(J-H) = 0.7$], and $A_V = 5.6 \pm 0.3$ [$E(J-K) = 0.95$], respectively, for the screen model. This reasoning may appear circular as it first needs to be shown that the parameters of the ring *are in fact* fitted by a starburst model before using starburst colors to infer an extinction correction. We will show below, however, that the basic conclusion (that the ring is a star formation region) does not depend on the details of the extinction adopted. It is evident that, while the $V-K$ color gives the same extinction as the Hβ/Brγ ratio, the longer wavelength colors imply higher extinctions, inconsistent with a simple screen.

As an alternative we consider a model where *gas and dust are fully mixed* (the "mixed" model), such as in the case where molecular/dust clouds and active star formation regions are embedded in the same volume. In that case the extinction attenuation at frequency ν scales as $\{1 - \exp[-\tau_{\mathrm{dust}}(\nu)]\}/\tau_{\mathrm{dust}}(\nu)$ (e.g., Thronson et al. 1990). Figure 6 shows the dependence on A_V of the reddening $E(X-Y)$ between various wavelengths X and Y, ranging from 0.5 to 2.2 μm in both the mixed and screen models. From Figure 6 and the observed reddening values given above, we then find $A_V = 13 \pm 3$ from $V-K$, $R-K$, and Hβ − Brγ, $A_V = 25 \pm 13$ from $J-K$ (and $J-H$), and $A_V > 10$ from Hα − Hβ. While this model does not provide a perfect solution with a single, well-defined A_V either, the agreement of observed reddening at different wavelengths is significantly better than for the screen model. Similar conclusions were obtained by McLeod et al. (1993) in their study of the starburst galaxy M82. As discussed above (§ 3.2), the mixed model is also suggested by the relative spatial distributions of the various tracers. We henceforth adopt a mixed model with $A_V \approx 15$.

We note that in terms of absolute fluxes the difference between a mixed model with $A_V = 15$ and a screen model with $A_V \approx 2.3$ is not large (Table 5). For instance, it results in a 50% upward correction of K-band flux density and Brγ flux. This correction changes the model results significantly in quantitative, but not in qualitative terms. The main consequence, however, is that the visible/near-infrared color information is lost for constraining the burst parameters. For large extinctions ($A_V \gg 1$), the influence of extinction on the colors is anyhow much larger than the small differences in intrinsic colors for most burst models discussed below.

While we use an average A_V value for dereddening and estimating the integrated starburst properties of the ring, the spatial variations of colors and the 11.7 μm dust map of Miles et al. (1994) clearly indicate substantial extinction variations from position to position, and the "redder" regions on the $J-K$ and $V-K$ maps of Figure 5 require very large extinctions indeed ($A_V \to \infty$ in the mixed model), consistent with the interpretation that much of the molecular gas implied by our maps and the CO observations of Meixner et al. (1990) is hidden there.

4.2. *Continuum Fluxes, Luminosities, and the Supernova Rate*

The key observed parameters of the circumnuclear ring of NGC 7469 are listed in Tables 3 and 4. Infrared line and continuum fluxes of the ring (integrated over radii from 0".7 to 2".5), along with those of the nucleus (radius ≤0".7) are given in Table 3, while other parameters taken from the literature and also separated into ring and nucleus are listed in Table 4. To obtain accurate flux densities of nucleus and ring at the different wavelengths we computed azimuthally integrated flux densities as a function of radius from the speckle maps presented in this paper and in Mauder et al. (1994). We derived an absolute calibration of the Mauder et al. (1994) data from the 17" aperture photometry of Wampler (1971). Figure 7 shows the derived spectral energy distributions for nucleus and ring, as well as for the entire galaxy, in beam sizes ranging from 8" to 60". In addition to the speckle data, we have included the 11.7 μm measurements of Miles et al. (1994), the 12, 25, 60, and 100 μm *IRAS* fluxes, and 3.5 and 4.8 μm photometry (Roche et al. 1991). The nucleus and ring contribute comparable fluxes

TABLE 4

PARAMETERS OF NGC 7469 TAKEN FROM LITERATURE

Parameter	Nucleus	Ring	Comments
V-band flux density (mJy)	8.4	6.3	From Mauder et al. 1994 maps and Wampler 1971 fluxes
R-band flux density (mJy)	11.5	10.8	From Mauder et al. 1994 maps and Wampler 1971 fluxes
Far-infrared luminosity ($L_\odot$)	3×10^{11}	1.5×10^{11}	Fig. 6
5 GHz radio flux density (mJy)	21	12	Wilson et al. 1991
Hβ flux (ergs s^{-1} cm^{-2})	1×10^{-13}	1.0×10^{-13}	Wilson et al. 1986
Hα flux (ergs s^{-1} cm^{-2})	...	6.7×10^{-13}	From Heckman et al. 1986; Wilson et al. 1991; Bonatto & Pastoriza 1991; with Hα/[N II] ≈ 1
[O III] λ5007 flux (ergs s^{-1} cm^{-2})	...	8.2×10^{-13}	Wilson et al. 1986
CO 1–0 flux (Jy km s^{-1})	40	160	Meixner et al. 1990

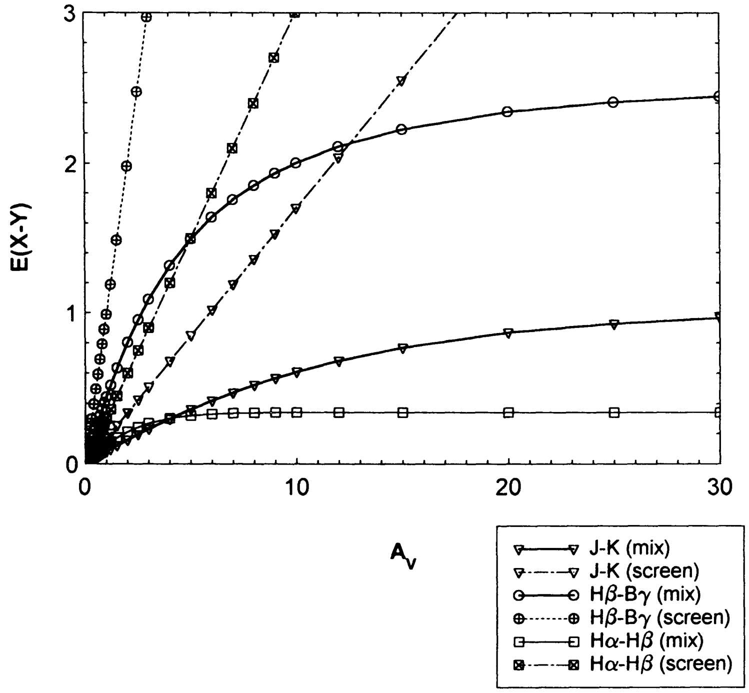

FIG. 6.—Reddening as a function of visual extinction A_V, for different combinations of wavelengths X and Y. Dotted and dash-dotted lines mark the case of a simple screen, while solid lines indicate that the dust is assumed to be fully mixed with the stars/gas. Triangles, circles, and squares denote the different wavelength combinations, as indicated in the inset.

between 0.5 and 1.6 μm. Extrapolating from the nuclear red near-infrared color, we find that it probably dominates the spectral energy distribution between 2 and ≤10 μm. This is likely caused in part by hot dust located very close to the central energy source. In addition there may also be significant contribution from a nonthermal power law from the central AGN (e.g., Westin 1985). At 11.7 μm the ring's contribution is again slightly greater than that of the nucleus. This implies that the ring contains a lot of cool dust whose emission probably dominates the total spectral energy distribution of the entire galaxy beyond 25 μm. With these inputs we can estimate the bolometric luminosities of the ring and the nucleus to be $3 \pm 0.5 \times 10^{11}$ $L_{\odot}$ and $1.5 \pm 0.5 \times 10^{11}$ $L_{\odot}$, respectively (Table 5).

TABLE 5

OBSERVED PROPERTIES OF NGC 7469 STARBURST RING[a]

	EXTINCTION MODEL[b]		
PARAMETER	$A_V = 2.3$ Screen	$A_V = 15$ Dust/Star/Gas Mixture	COMMENTS
$L_{\rm BOL}$ ($L_{\odot}$)	3×10^{11}	3×10^{11}	Bolometric luminosity (see § 4.2)
$L_K(0)$ ($L_{\odot}$)	2×10^9	3×10^9	Dereddened luminosity between 1.9 and 2.4 μm
$L_{\rm Lyc}(0)$ ($L_{\odot}$)	6×10^9	9.5×10^9	Dereddened $\lambda \leq 912$ Å luminosity from Brγ flux (2.2×10^{-14} ergs s^{-1} cm^{-2}) and $L_{\rm Lyc}(L_{\odot}) = 5.37 \times 10^{19} F_{\rm Br\gamma}$ (ergs s^{-1} cm^{-2})D(Mpc)^2
$\nu_{\rm SNR}$ (yr^{-1})	0.4	0.4	From $\nu = 3.7 \times 10^{-2} s_{5\,\rm GHz}(mJy)D$(66 Mpc)^2 (Völk 1989)
$L_{\rm BOL}/L_{\rm Lyc}(0)$	51 ± 8	33 ± 5	
$L_K(0)/L_{\rm Lyc}(0)$	0.33 ± 0.1	0.33 ± 0.1	
$10^9 \nu_{\rm SNR}/L_{\rm Lyc}(0)$	0.075	0.049	
$(V-K)$ (0)	1.75	1.68	Extrapolated from 5400 Å map of Mauder et al. 1994 and Wampler 1971 V flux
$(R-K)$ (0)	1.57	1.2	Extrapolated from 6660 Å map of Mauder et al. 1994 and Wampler 1971 R flux
$(J-K)$ (0)	1.06	0.69	
Gas mass in molecular clouds (R = 0″.7–2″.5)......	8.8×10^9 (X/X_G) $M_{\odot}$		From CO 1–0 flux and $X_G = N(\rm H_2)/I(\rm CO) = 2.3 \times 10^{20}$ cm^{-2} (K km s^{-1})$^{-1}$, corrected for 38% helium mass fraction (§ 4.3)
Dynamic mass ($R \leq$ 2″.5)	$(4.5 \pm 1) \times 10^9$ $M_{\odot}$		From stellar velocity dispersion $\sigma_* = 110 \pm 40$ km s^{-1} and gas rotation curve (§ 4.3)

[a] Where applicable, integrated between 0″.7 to 2″.5 from nucleus.

[b] See § 4.1; extinction curve of Draine 1989.

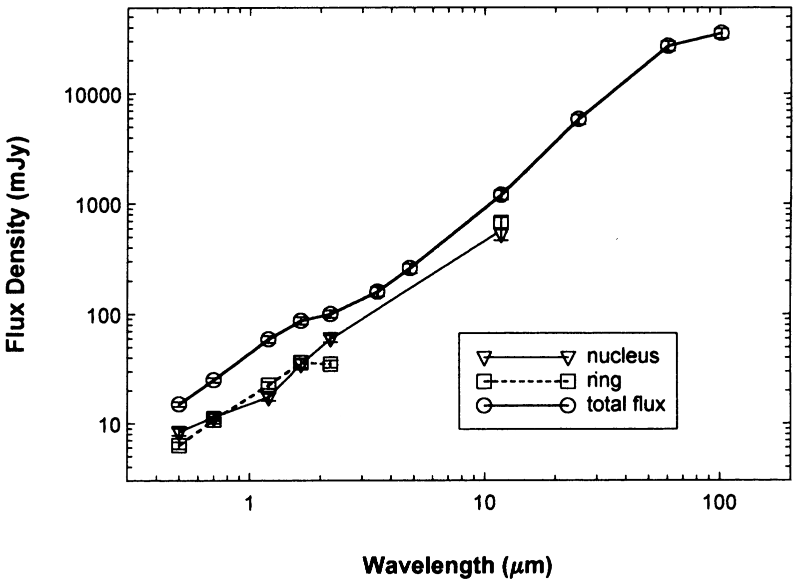

FIG. 7.—Visible/infrared spectrum of NGC 7469. Circles denote the total spectrum, taken from Wampler et al. (1971), Moorwood & Glass (1985), and Roche et al. (1991). Squares denote the spectrum of the circumnuclear ring (0".8 ≤ R ≤ 2".5) derived from the high-resolution data sets in this paper, Mauder et al. (1994), and Miles et al. (1994). Triangles denote the nuclear spectrum (R ≤ 0".8), taken from the same data sets.

Table 5 also lists the dereddened K-band and Lyman continuum luminosities and the supernova rate $\nu_{\rm SNR}$ under the assumption that $\nu_{\rm SNR} = 3.7 \times 10^{-2}\ S_{5\,\rm GHz}$(mJy) [or $\nu_{\rm SNR} = 2.5 \times 10^{4} L_{5\,\rm GHz}(L_{\odot}\ {\rm Hz}^{-1})$; see Condon 1992 for a discussion]. That conversion factor is derived from the assumption that the 5 GHz radio flux density is nonthermal (Wilson et al. 1991) and arises from supernova remnants with the proportionality factor derived from observations of M82 (Völk 1989) and NGC 1808 (KSG).

4.3. *Masses*

The *molecular gas* mass in the nucleus of NGC 7469 can be estimated from the CO 1–0 interferometric observations of Meixner et al. (1990, Table 4), an appropriate scale factor between CO flux and H_2 column density, and a 40% correction in mass for helium. The Galactic disk conversion factor from velocity-integrated CO 1–0 brightness to H_2 column density $X_G = H({\rm H_2})/I({\rm CO}) = 2.3 \times 10^{20}\ {\rm cm^{-2}}\ ({\rm K\ km\ s^{-1}})^{-1}$ (Strong et al. 1988) is strictly applicable only to a virialized molecular cloud medium of kinetic temperature $T \approx 10$ K and mean H_2 density $\langle n({\rm H_2})\rangle \approx 300\ {\rm cm^{-3}}$. Observations of other galaxies suggest that the interstellar medium (ISM) of starburst galaxies is warmer ($T \approx 25$–80 K; Harris et al. 1991; Genzel 1992; Güsten et al. 1993) and denser (Harris et al. 1991; Solomon, Downes, & Radford 1992). Still the Galactic disk conversion factor appears to work reasonably well also in several starburst galaxies (Eckart et al. 1990; R. Genzel, A. I. Harris, & A. Eckart 1994, private communication), probably because X scales with $[\langle n({\rm H_2})\rangle]^{1/2}/T$ so that the effects of higher density and temperature cancel each other to first order. However, in the center of M82, Wild et al. (1992) find $X \leq 10^{20}$, so that the molecular mass in that galaxy deduced with the Galactic ratio would be overestimated by a factor of 2–3. For NGC 7469 the data of Meixner et al. (1990) within a radius of 2".5 (800 pc) from the nucleus imply

$$M_{\rm GAS}(2''.5) = 1.1 \times 10^{10}(L_{\rm CO}/200\ {\rm Jy\ km\ s^{-1}}) \times (X/X_G)D(66\ {\rm Mpc})^2\ M_{\odot}\ . \quad (1)$$

Of this $2.2 \times 10^{9}(X/X_G)\ M_{\odot}$ is in the nucleus (40 Jy km s^{-1}; Meixner et al. 1990). The mass of ionized gas is only a small fraction of the neutral gas mass [$O(10^{-3})$; Meixner et al. 1990].

The *dynamical mass* contained in the ring can be estimated from the gas and stellar dynamics. Of all of the gasdynamics investigations (Burbidge et al. 1963; Anderson 1973; Wilson et al. 1986; DeRobertis & Pogge 1986), the Hα spectroscopy of DeRobertis & Pogge (1986) has the highest spatial (1".2) and spectral (55 km s^{-1}) resolutions. From their data, we infer a line-of-sight rotation velocity of 105 ± 15 km s^{-1} from the rotation curve along position angle 135°. Here we have corrected their published line center velocities for resolution effects (beam smearing). We calculated the line profiles for a thin, rotating ring (inner and outer radii 0".5 and 5", respectively) of different inclinations (25° to 47°), constant rotation velocity, and a Gaussian intensity distribution peaking at radius 1".5 that mimics the NGC 7469 ring. By convolving the kinematic profiles with the spatial and spectral profiles of DeRobertis & Pogge (1986) we found that their observed rotation velocity (95 ± 10 km s^{-1} at $R = 2''$) needs to be corrected upward by a factor between 1.04 for an inclination of $i = 25°$ and 1.14 for $i = 47°$, the latter being the inclination of the stellar disk at $R \geq 5''$ (Burbidge et al. 1963; Anderson 1973; DeRobertis & Pogge 1986). We thus find a rotation velocity of 146/(sin i/sin 47°) km s^{-1} and a dynamical mass within R = 2".5 (800 pc) of

$$M_{\rm DYN}({\rm gas\ rotation}) = (4 \pm 1) \times 10^{9} R(2''.5)/(\sin i/\sin 47°)^2\ M_{\odot}\ . \quad (2)$$

The stellar velocity dispersion in NGC 7469 can be estimated from the short-wavelength slope of the 2.3 μm CO overtone absorption bandheads presented in the spectra of Figures 2 and 3. For this purpose we convolved a template CO bandhead spectrum of a K5 giant with the instrumental response function and various stellar velocity dispersions until a satisfactory match with the NGC 7469 IRSPEC spectrum of the $v = 0$–2 band was reached. The best-fitting intrinsic line-of-sight velocity disperion is $\sigma_* = 110 \pm 40$ km s^{-1}. The corresponding dynamical mass is

$$M_{\rm DYN}(\text{stellar dispersion}) = 4.5^{+4}_{-2.7} \times 10^9 R(2''.5)\sigma_*(110)^2 \ M_\odot \ , \quad (3)$$

where we have assumed that the dispersion is isotropic. While the IRSPEC data refer to a 4''.4 × 8''.8 aperture, the 3D maps of the CO absorption depth (Fig. 2) show that most of the flux comes from the ring so that the measured dispersion is indeed characteristic of the stars at $R \approx 2''$. The masses from gas and stellar dynamics thus appear to agree well and are substantially smaller than the gas mass obtained from the CO 1–0 flux with a Galactic disk conversion factor.

Next we estimate the mass of the *old stellar component*. The ring/nucleus morphology immediately suggests that the near-infrared and visible emission samples a relatively young (≤ 1 Gyr) component. This is also the conclusion when considering the K-band flux. Taking nucleus and ring together, the dereddened absolute K-band magnitude of NGC 7469 is ≤ -25, 4.3 mag brighter than luminous "normal" spirals (Devereux, Becklin, & Scoville 1987). Thronson & Greenhouse (1988) have estimated the conversion factor from flux density to old stellar mass as

$$M_{\rm OLD} = 1 \times 10^9 \ aS(\text{mJy})D(66 \text{ Mpc})^2 \ M_\odot \ , \quad (4)$$

where $a = 1.1$ at K, 1.0 at J, 0.9 at H, and 1.3 at V. Equation (4) corresponds to an $M/L_{\rm BOL}$ ratio of ~ 2. With this conversion factor the observed near-infrared fluxes of ring and nucleus would correspond to "old" stellar masses of $(4 \pm 2) \times 10^{10}$ and $(3 \pm 1) \times 10^{10}$ $M_\odot$, respectively. This would imply a total "old" stellar mass an order of magnitude greater than the entire dynamical mass within 800 pc of NGC 7469. Dereddening (§ 4.3) would increase this mass further by 20%–90%. The old "bulge" component thus can only make a 10% contribution to the observed near-infrared/visible fluxes of NGC 7469. *Therefore, most of the near-infrared light in the ring is due to supergiants in the starburst.*

Perhaps the best indicator of the bulge component is the emission between nucleus and ring, at a radius of $\sim 0''.8$–$1''.2$. As pointed out above, this emission appears to have a relatively blue color, perhaps indicative of low extinction. Taking the J-band flux of this component as an example (2 ± 1 mJy), we estimate from equation (4) a mass of $M_{\rm OLD} = (2 \pm 1) \times 10^9$ $M_\odot$ within 2''.5 (800 pc) from the nucleus. For comparison, the mass enclosed within the central 800 pc of our own Galaxy is $(4\text{–}8) \times 10^9$ $M_\odot$ (Genzel & Townes 1987).

4.4. *Starburst Models*

We have used the deduced parameters of Table 5 as input parameters for a model of an evolving star cluster. We employed the model described by KSG, which is similar to other stellar population synthesis models (Larson & Tinsley 1978; Rieke et al. 1980, 1993; Gehrz, Sramek, & Weedman 1983; Scoville & Soifer 1991; Mas-Hesse & Kunth 1991; Doyon, Joseph, & Wright 1994) and includes the most recent stellar tracks for solar metallicity. It assumes an initial mass function (IMF) of lower mass cutoff m_l, upper mass cutoff m_u, and slope α defined in the usual way [$dN(M) = \text{const } M^{-\alpha} dM$ is the number of stars between M and $M + dM$ in the interval between m_l and m_u]. To calculate the integrated properties of the model star clusters, a star formation rate of time dependence $f(t)$ is assumed, along with the stellar evolution models of Maeder & Meynet (1988) and Schaerer et al. (1993). The results of Kurucz (1979) and Melnick, Terlevich, & Eggleton (1985) are used for calculating the Lyman continuum output of the massive stars. For a more detailed description we refer the reader to the Appendix of KSG.

The most important and best defined global input parameters constraining the star formation parameters are the Lyman continuum luminosity $L_{\rm Lyc}$ (measuring the present massive star formation rate), the bolometric luminosity $L_{\rm BOL}$, and the (extinction-corrected) K-band luminosity L_K. The ratios $L_{\rm BOL}/L_{\rm Lyc}$ and $L_K/L_{\rm Lyc}$ are measures (in slightly different ways) of time/evolution and shape of the IMF. It is evident that a smaller α (shallower slope of the IMF) can be exchanged to a large extent for a larger m_u and vice versa. The ratio $\nu_{\rm SNR}/L_{\rm Lyc}$ is a further time/IMF constraint somewhat similar in behavior to $L_K/L_{\rm Lyc}$. Both measure the number of moderate- and high-mass stars that have evolved off the main sequence. The ratio $\nu_{\rm SNR}/L_K$ in principle provides an independent constraint on the time evolution and IMF. It increases with time for the first $(1\text{–}2) \times 10^7$ years and then reaches a constant value in a constant star formation burst while it decreases again in a decaying burst as the supernova rate is sensitive to more massive stars (≥ 8 $M_\odot$) that disappear earlier than the giants/supergiants probed by the K-band emission. However, the conversion factor from radio luminosity to $\nu_{\rm SNR}$ also depends on the magnetic field energy density and the density of the ISM (see Völk 1989; Condon 1992) so that the supernova rate derived in this way is probably less reliable. We therefore treat $\nu_{\rm SNR}/L_{\rm Lyc}$ only as a secondary constraint and consistency check. Similarly, the 2.058 μm He I/Brγ line flux ratio depends on the (He$^+$)/(H$^+$) abundance ratio, which in turn is a function of the hardness of the radiation field and thus probes the uppermost part of the IMF. Doyon et al. (1992) have presented a quantitative analysis of this ratio and find that it indeed constrains the upper mass cutoff for $m_u \leq 50$ $M_\odot$. In contrast, Shields (1993) points out that the He I/Brγ ratio depends sensitively on many other parameters of the H II regions (density, dust content, and velocity structure) so that its value as a quantitative measure of m_u is questionable. Again, we have decided to use this diagnostic ratio retrospectively as a consistency check. Finally, the X-ray emission can be used as a constraint to the burst's age (Rieke et al. 1993) if it originates in an extended supernova-driven superwind, as in M82. The X-ray luminosity of NGC 7469 is substantial ($\geq 5 \times 10^9$ $L_\odot$; Piro et al. 1990), but its spatial extent is unknown and it is more probably connected with the central AGN.

4.4.1. *Models with a Constant Star Formation Rate*

Figure 8*a* shows m_u and burst age t as a function of $L_{\rm BOL}/L_{\rm Lyc}$, log $(L_K/L_{\rm Lyc})$, 10^9 $\nu_{\rm SNR}/L_{\rm Lyc}$, log $(R_*/L_{\rm Lyc})$, and log $(M_*/L_{\rm Lyc})$ for models with a constant star formation rate [$f(t) = \text{const}$] and $m_l = 1$ $M_\odot$. Here R_* is the total present-day star formation rate and M_* is the mass of stars formed since the beginning of the burst. Table 6 summarizes the derived burst parameters. In Figure 8*a* we show the possible range of fits for models with $\alpha = 2.5$ ($\approx$Salpeter IMF). Acceptable fits range from $m_u = 33$ $M_\odot$ and $t = 3 \times 10^7$ yr to $m_u = 60$ $M_\odot$ and $t = 5 \times 10^8$ yr. The large allowed range results from the fact that the $L_{\rm BOL}/L_{\rm Lyc}$ and $L_K/L_{\rm Lyc}$ curves run almost parallel to each other in much of the relevant part of the (m_u, t) phase space. Within this range the best fit for all diagnostic ratios, including the supernova rate estimated from the Völk (1989) $\nu_{\rm SNR}/L(5 \text{ GHz})$ conversion factor [$\nu_{\rm SNR}/L_{\rm NT}(5 \text{ GHz}) = 2.7 \times 10^4$ yr^{-1} Hz $L_\odot^{-1}$], is obtained for solutions with $m_u \approx 40$ $M_\odot$

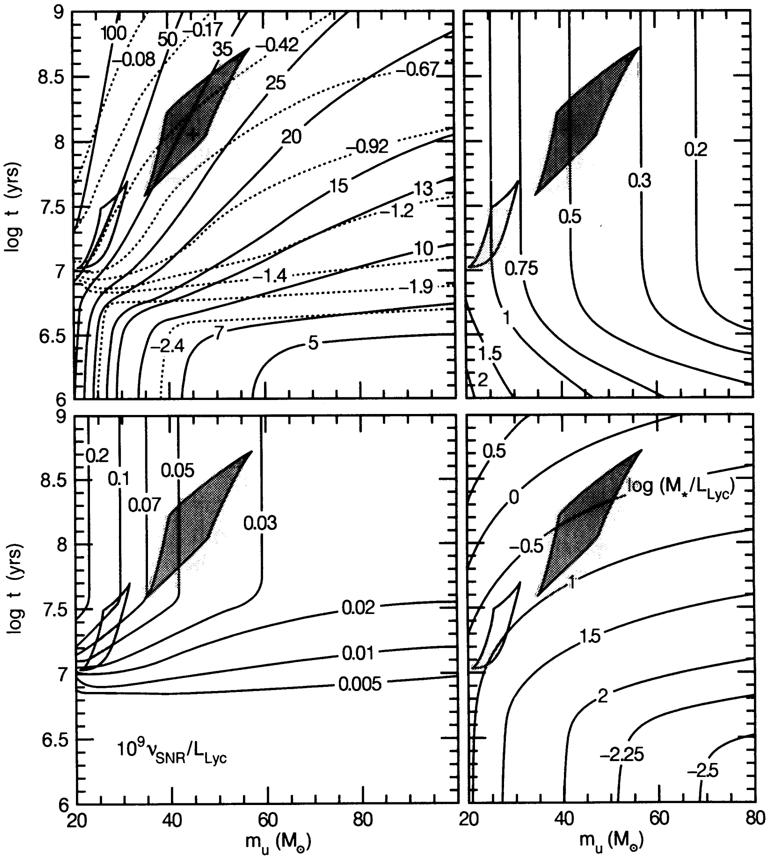

FIG. 8*a*

FIG. 8.—Results of starburst models. (*a*) Model calculations for constant star formation models ($\alpha = 2.5$). *Top left*: L_{BOL}/L_{Lyc} (*solid lines*) and log (L_K/L_{Lyc}) (*dashed lines*) as a function of m_u and burst age t in a starburst model with $f(t)$ = const and $\alpha = 2.5$. The constraints derived for the circumnuclear ring are indicated by a large cross (uncertainties shaded) for the "mixed" extinction ($A_V = 15$) and by a large triangle for a screen extinction ($A_V = 2.3$). *Top right*: log $(10^9 R_*/L_{Lyc})$. *Bottom left*: $10^9\ \nu_{SNR}/L_{Lyc}$. *Bottom right*: log (M_*/L_{Lyc}). (*b*) Same as (*a*) for an exponentially decaying model ($f(t) = \exp\,[-t/(5 \times 10^6 \text{ yr})]$, $\alpha = 2.5$). The shared region indicates the allowed zone for the circumnuclear ring in the "mixed" extinction scenario.

and $t \approx 10^8$ yr (Table 6). With the Condon & Yin (1990) conversion factor $[\nu_{SNR}/L_{NT}(5 \text{ GHz}) = 1.0 \times 10^4]$ solutions are favored with smaller m_u and smaller t ($m_u \approx 33\ M_\odot$ and $t = 2 \times 10^7$ yr). If instead of the mixed dust/stars case with $A_V = 15$ the screen solution with $A_V = 2.3$ is chosen, solutions with still smaller m_u ($\leq 30\ M_\odot$) and t ($\approx 1.5 \times 10^7$ yr) are indicated (Fig. 8*a*). If instead of $\alpha = 2.5$ a flatter IMF is chosen ($\alpha = 1.5$), as proposed for M82 by Rieke et al. (1993), naturally the solutions have smaller upper mass cutoffs as compared to the $\alpha = 2.5$ case ($m_u \leq 30$ instead of 40 $M_\odot$) and the resulting burst ages are smaller ($t \approx 10^{7.1}$ yr; Table 6).

The ring parameters can be *well matched by constant star*

TABLE 6

DERIVED PROPERTIES OF STARBURST IN THE NGC 7469 RING[a]

PARAMETER	CONTINUOUS STAR FORMATION $\alpha = 2.5$, $A_V = 15$ Mixed Extinction	 $\alpha = 2.5$, $A_V = 2.3$ Screen Extinction	 $\alpha = 1.5$, $A_V = 15$ Mixed Extinction	EXPONENTIAL DECAY ($t_s = 5 \times 10^6$ yr) $\alpha = 2.5$, $A_V = 15$ Mixed Extinction
Burst age	$10^{8\pm0.6}$	$10^{7.1\pm0.7}$	$10^{7.6\pm1.5}$	$10^{7.2\pm0.1}$
m_u ($M_\odot$)	43^{+18}_{-10}	23^{+10}_{-3}	28 ± 5	≤ 100
L_{BOL}/L_{Lyc}	35 ± 5	51 ± 8	35 ± 5	40 ± 5
L_K/L_{Lyc}	0.33 ± 0.1	0.33 ± 0.1	0.33 ± 0.1	0.2 ± 0.1
ν_{SNR} (yr^{-1})	0.42 ± 0.15	0.45 ± 0.2	0.55 ± 0.2	0.7 ± 0.3
$\nu_{SNR}/L_{(5\text{ GHz})}$[b] (yr^{-1} Hz $L_\odot^{-1}$)	$(2.4 \pm 1) \times 10^4$	$(3 \pm 1.5) \times 10^4$	$(3.5 \pm 2) \times 10^4$	$(4.4 \pm 2) \times 10^4$
R_* ($M_\odot$ yr^{-1})	28 ± 10	65 ± 20	20 ± 7	180 ± 60
M_* ($M_\odot$)	$(2 \pm 1) \times 10^9$	$(7 \pm 3) \times 10^8$	$(6 \pm 3) \times 10^8$	$(6 \pm 3) \times 10^8$
M_*/M_{GAS}	$0.2 \pm 0.1(X_G/X)$	$0.1 \pm 0.05(X_G/X)$	$0.1 \pm 0.05(X_G/X)$	$0.1 \pm 0.05(X_G/X)$
$(M_* + M_{GAS} + M_{OLD})/M_{DYN}$[c]	3.3	3	3	3

[a] All models assume $m_l = 1\ M_\odot$, $L_{BOL} = 3 \times 10^{11}\ L_\odot$.

[b] $L_{(5\text{ GHz})}$ is the nonthermal 5 GHz luminosity density $L_{(5\text{ GHz})} = 1.35 \times 10^{-6}\ S_{5\text{ GHz}}(\text{mJy})\ D(66\text{ Mpc})^2$.

[c] $M_{OLD} = 2 \times 10^9\ M_\odot$, $M_{GAS} = 11 \times 10^9\ M_\odot$ for $X = X_G$, $M_{DYN} = 4.5 \times 10^9\ M_\odot$ within 2".5 of the nucleus.

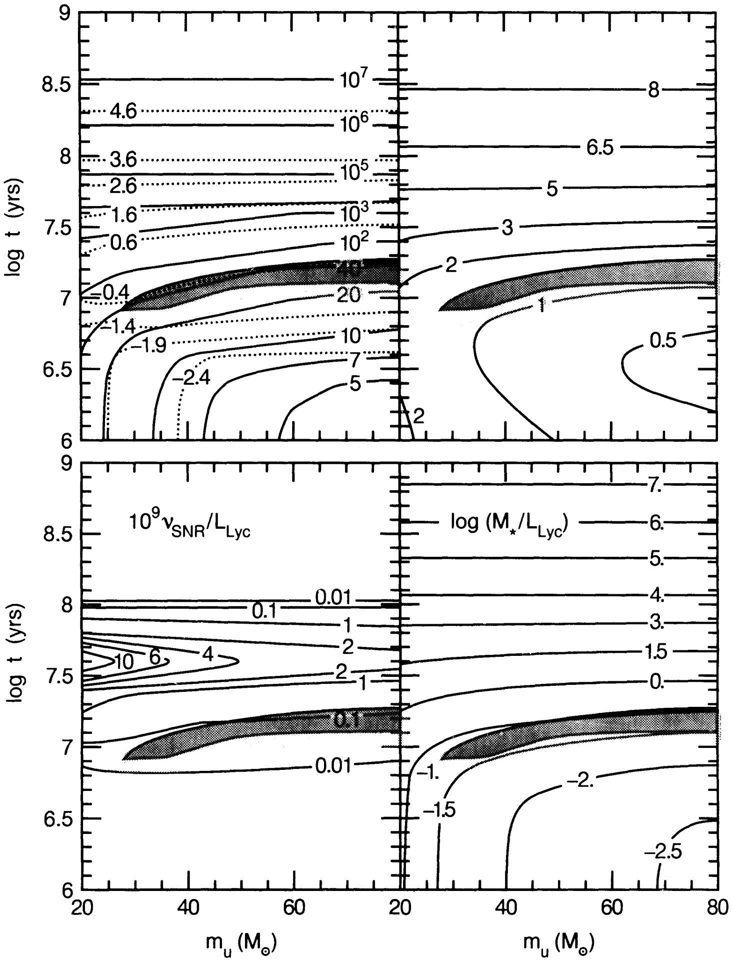

FIG. 8b

formation models with best estimate ages of several 10^7 yr to 10^8 yr and relatively small upper mass cutoffs ($m_u \approx 30$–40 $M_\odot$). This range of upper mass cutoffs would also be consistent with the relatively low observed 2.058 μm He I/Brγ ratio (0.35) if we apply the model of Doyon, Puxley, & Joseph (1992). We do note that the conclusion of a lack of the most massive stars does strongly depend on present stellar atmospheric models (for solar metallicity) and the assumption of little nebular absorption in the Lyman continuum. If the most massive stars in a fairly high metallicity burst (likely the case for NGC 7469) produce less Lyman continuum than assumed in those models, or if dust in the H II regions absorbs a significant fraction of the Lyman continuum radiation emitted by the stars, the upper mass cutoffs required in our models would have to be corrspondingly greater.

4.4.2. *Decaying Models*

As the other extreme we have also investigated models with a star formation rate that is rapidly decaying with time, $f(t) = \exp(-t/t_s)$. As a specific case we show in Figure 8*b* the derived burst parameters for a decay time of $t_s = 5 \times 10^6$ yr. Since this time is smaller than the lifetime of all but the most massive stars, the model basically describes a one-time, "delta" burst. As the dependence on the exponential decay of the star formation rate overwhelms the dependence on m_u, the model results change very little with varying m_u. Figure 8*b* and Table 6 show that reasonable (but not perfect) simultaneous fits to $L_{\rm BOL}/L_{\rm Lyc}$, $L_K/L_{\rm Lyc}$, and $\nu_{\rm SNR}/L_{\rm Lyc}$ can be found for $t \approx 1.5 \times 10^7$ yr and a range of m_u. In other words, the decaying burst model has the *intriguing virtue that there needs to be no cutoff in the largest stellar masses formed in the burst.* The "low excitation" of the burst, including the low He I/Brγ ratio, is in this case the natural result of the fact that the most massive stars have already disappeared. The conclusions about star formation rate and burst mass are in this case very similar to the $f(t) =$ const case (Table 6). A short-duration burst that took place a few million years ago is probably also the best explanation for the low excitation and stellar population in the cluster at the center of our own Galaxy (Genzel, Hollenbach, & Townes 1994b). Moreover, short-duration bursts have been favored for "Wolf-Rayet" starburst galaxies by Conti & Vacca (1993, 1994) and for M82 by Rieke et al. (1993).

4.4.3. *Gas Mass and Lower Mass Cutoff*

Table 6 shows that the ratio $\xi = (M_* + M_{\rm GAS} + M_{\rm OLD})/M_{\rm DYN} \approx 3$; that is, the sum of stellar and gas mass appear to significantly exceed the dynamical mass. This conclusion holds independent of extinction model, or IMF slope, or of star formation history. It also does not depend very much on the lower mass cutoff used in the IMF. Table 6 uses $m_l = 1$ $M_\odot$, and the mass in the burst scales approximately with $m_l^{-0.6}$ (for $\alpha = 2.5$) so that a change in m_l up or down by a factor of 2 changes M_* down or up by a factor of 1.5. However, the burst mass is a relatively small (10%–40%) contribution to the dynamic mass. $M_{\rm OLD}$ and $M_{\rm GAS}$ dominate and are uncertain, so that the present data do not constrain m_l. Specifically ξ does not decrease significantly by increasing m_l. Therefore, in contrast to M82 (Rieke et al. 1980, 1993) and perhaps NGC 3256 (Doyon et al. 1994) there is no need to postulate that star formation in the ring of NGC 7469 is biased toward high-mass stars.

The dilemma is rather that ξ is significantly greater than 1, because the gas mass for $(X/X_G) = 1$ is already by itself greater than the deduced dynamical mass. To bring ξ down to 1, either X can only be $\sim(0.2 \pm 0.1) \times X_G$, or the dynamical mass has been underestimated by about a factor of 3. The latter explanation would require that the inclination of the ring is significantly less than the disk of NGC 7469 at $R \geq 5''$ (25° instead of 47°) and simultaneously that the stellar velocity dispersion is anisotropic by the same factor. This possibility is perhaps supported by the circular morphology of the ring and by our argument in § 4.3 that most of the stellar light is due to the (young) ring starburst. The former explanation (small conversion factor from CO 1–0 flux to H_2 column density) appears even more plausible given the very large energy density due to OB star radiation and winds and supernova explosions to which the molecular clouds in the ring of NGC 7469 are exposed. The mean UV energy flux at the surfaces of those clouds is $\sim 5 \times 10^4$ times the local interstellar radiation field in the solar neighborhood χ_0 ($\chi_0 = 2.5 \times 10^{-3}$ ergs cm^{-2} s^{-1}; e.g., Genzel 1992). This energy density is 40 times larger even than the average radiation field density in M82, where Wild et al. (1992) and Harris et al. (1991) deduce $X/X_G = 0.4$ and $T_{\rm GAS} \approx 40$–50 K. It is comparable to the core of the Orion star-forming region, where gas temperatures are 70–100 K and the CO 1–0 line samples the warm, photon-dominated surface layers of the molecular clouds, rather than their interiors. From an analysis similar to the present one, Shier, Rieke, & Rieke (1994) conclude that $X/X_G = 0.1$–0.25 in the luminous starburst galaxies NGC 1614, IC 694, and Arp 220. Therefore, we favor the explanation of a small conversion factor from CO flux to H_2 column density also for the NGC 7469 ring, keeping in mind that the alternative possibility of a small inclination angle can be tested by future high-resolution studies of the gasdynamics of the ring.

Depending now on the exact value of X/X_G, the ratio of stellar mass in the burst to (remaining) gas mass is either reasonably large (0.5–1 for $X/X_G \approx 0.2$) or fairly small (0.1–0.3 for $X/X_G \approx 1$). In the former, and in our opinion more likely, case the gas reservoir is about to be exhausted and the burst to be terminated with a high star formation efficiency, for both continuous and decaying burst models. This convergence is very satisfactory and simultaneously provides a natural explanation of why the burst is terminating. If X/X_G is large, however, the burst may still continue for much longer than its present age (for the continuous burst models), or have a low star formation efficiency (for the decaying burst).

4.4.4. *Summary*

In summary then of this entire section on the star formation properties of the NGC 7469 ring, we conclude that the visible, infrared, and radio observations are all in excellent agreement with the *hypothesis of a powerful circumnuclear burst.* We have shown that this burst likely accounts for $\sim\frac{2}{3}$ of the total luminosity of NGC 7469. Its relatively "low excitation" can be explained either by constant formation where the most massive stars are (presently) not forming or, perhaps more plausibly, by a decaying burst that is about to terminate. Adopting as our working hypothesis that the conversion factor between CO line flux and H_2 column density is significantly smaller than in the Galactic disk, the star formation efficiency in NGC 7469 is high and the burst is soon going to terminate simply due to exhaustion of the gas reservoir. The starburst originates in a number of supergiant star formation regions which have absolute K-magnitudes of about -19. Assuming that the majority of the 2 μm light is produced by red supergiants of $M_K = -8$ to -11, this implies about $O(10^4)$ red supergiants per such region. In addition these regions contain a few 10^4 OB stars each ($L_{\rm Lyc} \approx 2.5 \times 10^8\ L_\odot$), 10–100 times the stellar content of the 30 Dor star formation region in the LMC (Walborn 1991) and at the upper end of giant extragalactic star formation (H II region) complexes (Kennicutt 1991).

4.5. *What Has Triggered the Burst?*

An important issue that needs to be addressed is the cause of the massive circumnuclear starburst in NGC 7469. As is postulated in cases of pure starburst galaxies, the cause for the starburst in NGC 7469 may be the response of the molecular ISM to an interaction of NGC 7469 with its neighbor [IC 5283, which lies at a (projected) distance of $\approx 83''$ or 27 kpc; Burbidge et al. 1963], or to a central bar (Wilson et al. 1991). The high-resolution SHARP maps are a very good way of testing the bar hypothesis, as the evolved/old stellar population in the bar should be most easily visible in the near-infrared (Pompea & Rieke 1990). However, Figure 1 does not show evidence for a (nonaxisymmetric) bar structure inside of the ring, with an upper limit of $\sim 0.75\%$ of the nuclear peak. For comparison, if the stellar bar in NGC 1068 (e.g., Scoville et al. 1988; Thronson et al. 1989) were moved to the distance of NGC 7469 and observed at 0."4 resolution, the ratio of bar to nuclear flux at a radius of 1" would be ~ 0.02, comparable to the strongest emission in the NGC 7469 ring. Hence, a bar of the same relative strength as that in NGC 1068 should have been clearly detectable on the K-band SHARP map. The nuclear luminosities of NGC 1068 and NGC 7469 are quite comparable, and NGC 1068 also has a star-forming ring at a radius of 880 pc.

For completeness we note that Mazzarella et al. (1994) do claim to have found a bar by considering the nonaxisymmetric residuals of their $\approx 0."8$ near-infrared images. They find excess power northeast and southwest of the nucleus and interpret this as a bar. Our J- and K-band images in Figure 1 show the same asymmetry, but it is caused by the northeast and southwest sections of the ring/spiral-arm system being the brightest. The difference in interpretation can thus be entirely ascribed to the lower resolution of the Mazzarella et al. measurements.

Perhaps the most likely cause for the starburst thus is the tidal interaction with IC 5283. IC 5283 shows a perturbed structure with knots and tidal tails (Burbidge et al. 1963; Marquez & Moles 1994), a clear signature of a strong interaction. The morphology of these tails and the distance and the relative velocity between NGC 7469 and IC 5283 [O(100 km s^{-1}); Burbidge et al. 1963] all point to an onset of the interaction more than 1.5×10^8 yr ago. Our best burst age estimates are smaller and perhaps *much* smaller than this time. Therefore, either the present burst in NGC 7469 is not the original burst triggered by the interaction, or we are witnessing a large delay between initial tidal perturbation and onset of star formation activity. Such a delay could be the result of the perturbed gas having to first stream into and settle at the position of the inner Lindblad resonance (i.e., the ring) and within the nucleus (see Doyon et al. 1994). Vazquez & Scalo (1989) have argued that delayed bursts in fact are expected from the consideration that cloud-cloud collisions initially shred and disperse the molecular cloud systems in interacting galaxies. In their models rapid, large-amplitude bursts follow a relatively long "gestation" period.

5. GAS AND STAR FORMATION IN THE NUCLEUS

This section contains a discussion of the molecular and coronal gas in the central arcsecond and addresses the question whether there is evidence for star formation in the nucleus itself.

5.1. *Molecular Gas in the Nucleus*

Our H_2 maps with 3D and FAST (Figs. 2 and 4) present for the first time direct evidence for the presence of molecular gas in the nuclear region of a classical Seyfert 1 galaxy (inner NLR, radius $\leq 10^2$ pc). Assuming that the vibrationally excited H_2 is thermally excited with a temperature near 2000 K, the nuclear flux corresponds to $2 \times 10^3\ M_\odot$ of hot molecular hydrogen. If the ratio of total molecular hydrogen to hot molecular hydrogen is 10^4–10^5, as in NGC 1068 (Rotaciuc et al. 1991; Blietz et al. 1994), the total H_2 mass within $\approx 10^2$ pc of the nucleus of NGC 7469 may range between 2×10^7 and $2 \times 10^8\ M_\odot$. The highest resolution 2.6 mm CO 1–0 interferometric data ($2'' \times 3''$) of Meixner et al. (1990) indicate that the H_2 mass in the central beam is about $1.6 \times 10^9 (X/X_G)\ M_\odot$. If the ≈ 500 mJy 11.3 μm flux density observed in a $0\farcs7$ beam toward the nucleus of NGC 7469 by Keto et al. (1992) and Miles et al. (1994) can be interpreted in terms of dust emission, the nuclear 10 μm dust luminosity of NGC 7469 is about half that of NGC 1068 (Cameron et al. 1993). From a detailed dust model of NGC 1068, Cameron et al. (1993) deduce a total nuclear gas mass of $1.5 \times 10^8\ M_\odot$, for a gas-to-dust mass ratio of 100. Since the nuclear parameters (luminosity and size scale) in NGC 7469 are quite similar to those of NGC 1068, another plausible estimate of the gas mass in NGC 7469 then is $\approx 8 \times 10^7\ M_\odot$, obtained by scaling the NGC 1068 mass with the ratio of nuclear 10 μm luminosities. While all three estimates are uncertain, they indicate clearly that the Seyfert 1 nucleus of NGC 7469 contains a large amount of dense, molecular gas and dust, comparable to that contained in a similar volume in the Seyfert 2 galaxy NGC 1068 (Rotaciuc et al. 1991; Blietz et al. 1994; Tacconi et al. 1994). The Seyfert 1 nucleus of NGC 7469 thus fits in with recent unifying scenarios which predict that dense, dusty molecular disks/tori are present in all AGNs and produce aspect-angle–dependent obscuration of short-wavelength radiation (e.g., Antonucci 1993). The unifying models would predict in the case of NGC 7469 that the view to the BLR/central X-ray source is unostructed because the dusty molecular cloud layer is seen more nearly pole-on.

5.2. *Physical Conditions in the Coronal-Line Region*

We have shown above (§ 3.4) that the infrared coronal-line emission in NGC 7469 predominantly arises from blueshifted gas in the intermediate velocity region (intermediate line region [ILR]; 300–1000 km $\mathrm{s^{-1}}$) at a radius ≤ 150 pc from the nucleus. Coronal-line emission may either arise in moderate-temperature [$T_e = (1\text{–}3) \times 10^4$ K] photoionized gas (Osterbrock 1969; Grandi 1978; Korista & Ferland 1989), or in hot ($T_e \approx E_{\mathrm{ionization}}/k \approx 10^6$ K) collisionally excited gas (Oke & Sargent 1968; Nussbaumer & Osterbrock 1970). In either case, the upper fine structure level of Si VI ($^2P_{1/2}$, Einstein *A*-coefficient 2.37 $\mathrm{s^{-1}}$) is then collisionally excited from the lower level ($^2P_{3/2}$), with critical densities of $n_{\mathrm{crit}} = 8 \times 10^8$ $\mathrm{cm^{-3}}$ at log $T_e = 5.6$ and $n_{\mathrm{crit}} = 10^8$ at log $T_e = 4.0$ (the collision strength of the transition is ~ 0.6; Greenhouse et al. 1993). For collisional excitation the Si VI ionization state has maximum fractional population [$x(\mathrm{Si\ VI}) = \{\mathrm{Si\ VI}\}/\{\mathrm{Si}\} = 0.65$] at log $T_e = 5.6$ (Shull & van Steenberg 1982; Greenhouse et al. 1993). In the case of photoionization the maximum fractional abundance is $x(\mathrm{Si\ VI}) \approx 0.2$ (Greenhouse et al. 1993). With these inputs the flux of the 1.96 μm [Si VI] line at distance D(66 Mpc) becomes

$$F([\mathrm{Si\ VI}]) \leq 10^{-24}\, \delta_{\mathrm{Si}} f_V\, \mathrm{EM}_V(\mathrm{cm^{-6}\ pc^3})\ \mathrm{ergs\ s^{-1}\ cm^{-2}}\ . \tag{5}$$

Here δ_{Si} is the gas phase abundance of Si relative to the solar abundance (3.5×10^{-5}). The abundance δ_{Si} would be significantly less than unity if Si were depleted on dust grains, as in the local Galactic ISM. EM_V is the volume emission measure ($\mathrm{EM}_V = \int n_e^2\, dV$), and f_V is the volume filling factor of [Si VI]-emitting gas in the beam ($1''$ or 320 pc at 66 Mpc). Note that to first order the flux is independent of the excitation mechanism (photoionization vs. collisional ionization) and the less than or equal sign indicates that the assumptions are optimistic; that is, $x(\mathrm{Si\ VI})$ is likely smaller than the largest values cited above and used in equation (5).

Assuming that the $1''$ beam contains a spherical emission region of rms electron density $\delta n_e = (\langle n_e^2 \rangle)^{1/2}$ the observed [Si VI] flux in NGC 7469 [corrected for H_2 *S*(3) emission; Table 3] requires

$$\delta n_e \geq 42\{F([\mathrm{Si\ VI}])/3 \times 10^{-14}\ \mathrm{ergs\ s^{-1}\ cm^{-2}}\} \times f_V^{-1/2}\, \delta_{\mathrm{Si}}^{-1/2}\ \mathrm{cm^{-3}}\ . \tag{6}$$

The mass of hydrogen nuclei in the coronal-line region (CLR) on NGC 7469 then is $2.5 \times 10^7 f_V^{1/2}\, \delta_{\mathrm{Si}}^{-1/2}$ ($M_\odot$), and the hydrogen column density of the CLR is $6 \times 10^{22} f_V^{-1/6}\, \delta_{\mathrm{Si}}^{-1/2}$ ($\mathrm{cm^{-2}}$), a significant fraction of the total (molecular) interstellar gas mass unless $f_V \ll 1$. Most of the [Si VI] emission comes from a region of intrinsic size smaller than $0\farcs5$, increasing the lower limit to the rms electron density in the CLR by a factor of 3. Any reddening further increases this density. The low extinction to the BLR of NGC 7469 ($\mathrm{A}_V \leq 0.6$) and the lack of large soft X-ray absorption (e.g., Brandt et al. 1993) would require that the filling factor of the CLR is still smaller and the rms electron density still larger.

Assuming that the similar line profiles and blueshifts of broad Brγ and [Si VI] lines in fact indicate that both lines emerge from the same region, the Brγ-to-[Si VI] flux ratio can be used to obtain an estimate of $x(\mathrm{Si\ VI})\delta_{\mathrm{Si}}$ if the photoionized model applies:

$$x(\mathrm{Si\ VI})\delta_{\mathrm{Si}} = 0.03\{F([\mathrm{Si\ VI}])/F(\mathrm{Br}\gamma)\}\{f_V(\mathrm{Br}\gamma)\}/f_V([\mathrm{Si\ VI}])\ . \tag{7}$$

With $x(\mathrm{Si\ VI}) \leq 0.2$ (Greenhouse et al. 1992; Oliva et al. 1994), $\delta_{\mathrm{Si}} \geq 0.15$, supporting our assumption above of a reasonably large gas phase abundance of Si in the CLR.

Another interesting constraint may come from [O III] λ5007. As mentioned above this line also shows blueshifted emission ($v_{\mathrm{hel}} = 4480$ km $\mathrm{s^{-1}}$) of about the same width as that of [Si VI] (Bonatto & Pastoriza 1990). The [O III]/Hβ ratio in the ILR is 0.6, significantly smaller than its value in the NLR (≈ 3.7; Bonatto & Pastoriza 1990). This suggests perhaps that the rms electron density in the ILR is near the critical density of the ^2D state of [O III] (7×10^5 cm^{-3}). If applicable to [Si VI], this estimate would imply high densities and a very low filling factor ($f_V \approx 10^{-8}$).

In summary, then, we conclude that the *coronal-line emission in NGC 7469 comes from fairly dense* ($\delta n_e = 10^2$–10^6 cm^{-3}), *intermediate-velocity gas of high* Si *gas phase abundance, within* $\leq 10^2$ pc *of the nucleus.* Oliva et al. (1994) have arrived at similar conclusions for the CLR in the Circinus galaxy. The present observations cannot yet distinguish between collisional and photoionization models of the CLR. The electron densities derived above are, however, near or above the upper limit of the allowed range in the photoionization models of Korista & Ferland (1989) which assume a low-density ISM on scales of 100–1000 pc. We conclude that this model does not adequately describe the nature of the CLR in NGC 7469.

The significant blueshift of the coronal lines (relative to the extended narrow-line gas) has commonly been interpreted as evidence for dust extinction toward the CLR (e.g., Penston et al. 1984). The brightness of the [Si VI] line (and other infrared coronal lines; Oliva et al. 1994), however, seems to exclude a large amount of dust (and hence depeletion) *within* the CLR (Oliva et al. 1994, eq. [8]) unless the [Si VI] emission has a very small filling factor. Furthermore, the fact that the blueshift of the infrared and visible coronal lines is about the same in all galaxies observed so far suggests that either the extinction is very small ($A_V \ll 1$, implying the same asymmetric gas distribution in all galaxies!) or very large ($A_V \gg 10$), with sharp edges.

The blueshift can be explained in a scenario of net outflowing gas if the coronal medium is extended and dusty and the net dust optical depth toward the blueshifted gas is less than that of the redshifted gas. The blueshift can also be explained in a scenario of net inflowing gas if the coronal gas originates from the surfaces of dense, dusty clouds. The CLR can then only be seen with low extinction toward the blueshifted clouds whose coronal gas surface is turned toward us (see Penston et al. 1984). Taking the above arguments together it would then appear that *the present data are more consistent with a scenario in which the coronal gas is located on the surfaces of dense, high column density (molecular?) dusty clouds that are streaming toward the center of NGC 7469.*

5.3. *Star Formation in the Nucleus*

One question that still needs to be discussed is the origin of the nuclear luminosity ($\approx 1.5 \times 10^{11}$ $L_\odot$) itself. Taken at face value the integral parameters and diagnostic ratios [$L_{\rm BOL}/L_{\rm Lyc}$, $L_K/L_{\rm Lyc}$, $\nu_{\rm SNR}(L(5\ {\rm GHz}))/L_{\rm Lyc}$] of the nucleus are similar to those of the ring and thus can in principle be explained by star formation. Correcting for an assumed extinction of $A_V = 2$ or a mixed model with $A_V \approx 15$, in analogy to the ring, the derived ratios are $L_{\rm BOL}/L_{\rm Lyc} = 20$–$31$, $L_K/L_{\rm Lyc} = 0.6$, and $10^9 \nu_{\rm SNR}/L_{\rm Lyc} = 0.09$–$0.14$, within a factor of 2 of the ratios for the ring (Table 5). In fact, these values can be met reasonably well by a constant star formation model of fairly large age ($t \geq 10^9$ yr) and relatively large upper mass cutoff ($m_u \approx$ 60–100 $M_\odot$). However, unlike in the ring, the observed colors of the nucleus ($V-K = 4.1$, $R-K = 3.5$, $J-H = 1.2$, and $J-K = 1.1$) cannot be matched by a starburst model with any reasonable extinction model (mixed or screen) and rather match colors of extincted AGNs (e.g., Armus et al. 1994). This can be easily seen from the spectral energy distribution in Figure 7 that shows that the nuclear colors are similar to the ring between V and H but then the $H-K$ color is very much redder than that of the ring. We have mentioned in § 4.2 that this probably indicates that a substantial fraction of the nuclear K-band flux is due to hot dust and/or a nonthermal power law. Consistent with this interpretation, the CO bandhead depth measured with 3D is ≤ 0.05 (Fig. 2), at least 3 times smaller than in the surrounding ring.

Concluding then that most of the nuclear infrared luminosity is nonstellar, the following arguments suggest that stars may contribute some fraction of the nuclear luminosity. Assuming that stellar emission from the nucleus would have about the same near-infrared colors as that of the ring, the spectral energy distribution in Figure 7 suggests that about one-third to half of the K-band flux might be stellar. From the equivalent width of the 3.1 μm PAH emission feature toward the nucleus (as compared to the ring), Mazzarella et al. (1994) estimate that about 17% of the nuclear 3.1 μm flux and 33% of the K-band flux is stellar, although these values are upper limits if one takes into account that PAH emission may be emitted along the line of sight to the nucleus but exterior to it. Finally, from the spatial distribution of the 11.3 μm flux (again compared to the ring) Miles et al (1994) conclude that no more than 20% of its flux comes from the nucleus, implying a similar limit to the fraction of star formation luminosity. If 15%–30% of the nuclear luminosity (4×10^{10} to 8×10^{10} $L_\odot$) is stellar with diagnostic ratios approximately as given above, the nucleus may be the site of continuous star formation occuring at a ratio of a few $M_\odot$ yr^{-1}.

In summary then, NGC 7469 appears to be an example of a luminous *IRAS* galaxy/classical Seyfert 1 galaxy that is predominantly (70%–80%) powered by star formation. The AGN may " only " be responsible for $\sim 10^{11}$ $L_\odot$.

6. CONCLUSIONS

New high-resolution near-infrared imaging and imaging spectroscopy of the nucleus of the infrared luminous Seyfert 1 galaxy combined with imaging and spectroscopy in the radio and visible bands, show that:

1. Most of the bolometric luminosity of the galaxy originates from a powerful starburst in a ring ≈ 500 pc from the center.
2. The age of the starburst is a few 10^7 yr, and it may presently be decaying because its gas reservoir is exhausted.
3. The most likely triggering mechanism for the burst is the interaction with NGC 7469's neighbor, IC 5283, in which case the present burst occurred with a $\geq 10^8$ yr delay from the onset of interaction.
4. Characteristics of a starburst galaxy and an AGN are found simultaneously in the same system.
5. There is a large concentration of interstellar (molecular) gas, a significant fraction of which is located within the NLR on scales of $\leq 10^2$ pc.
6. The conversion factor from CO 1–0 line flux to H_2 column density is likely significantly smaller than in the Galactic disk, presumably as the result of stellar radiation, winds, and supernova explosions strongly affecting the physical characteristics of the molecular cloud medium.
7. The coronal-line emission originates in fairly dense ($n_e \approx$ 10^2–10^6 cm^{-3}) gas in the intermediate velocity zone at $\leq 10^2$ pc from the nucleus. The observations favor a model in which

the coronal gas is on the surface of dense, dusty clouds that are streaming toward the nucleus.

In addition to the authors, A. Eckart, R. Hofmann, and B. Sams contributed to the SHARP program and/or participated in the SHARP observations. S. Drapatz, V. Rotaciuc, and P. P. van der Werf participated in the FAST observations. H. Kroker and N. Thatte helped making the first 3D observations a success. We thank all these colleagues without whom the present observations would not have been possible. We are grateful to the staffs of the William Herschel Telescope (operated by the Royal Greenwich Observatory), the ESO New Technology Telescope, and the Calar Alto Observatory (operated by the Max-Planck-Institut für Astronomie, Heidelberg) for their excellent support. W. Mauder, J. Miles, T. Helfer, and J. M. Mazzarella kindly provided us with electronic versions of their results. We thank our referee for very useful comments. We acknowledge support from the German-Israel Foundation.

REFERENCES

Aitken, D. K., Roche, P. F., & Phillips, M. M. 1981, MNRAS, 196, 101P
Anderson, K. S. 1973, ApJ, 182, 369
Antonucci, R. 1993, ARA&A, 31, 473
Armus, L., Surace, J. A., Soifer, B. T., Matthews, K., Graham, J. R., & Larkin, J. E. 1994, AJ, 108, 76
Blietz, M. 1994, Ph.D. thesis, Ludwig-Maximilian-Univ. München
Blietz, M., Cameron, M., Drapatz, S., Genzel, R., Krabbe, A., van der Werf, P. P., Sternberg, A., & Ward, M. 1994, ApJ, 421, 92
Bonatto, C. J., & Pastoriza, M. G. 1990, ApJ, 353, 445
Brandt, W. N., Fabian, A. C., Nandra, K., & Tsuruta, S. 1993, MNRAS, 265, 996
Burbidge, E. M., Burbidge, G. R., & Prendergast, K. H. 1963, ApJ, 137, 1022
Cameron, M., Storey, J. W. V., Rotaciuc, V., Genzel, R., Verstraete, L., Drapatz, S., Siebenmorgen, R., & Lee, T. J. 1993, ApJ, 419, 136
Condon, J. J. 1992, ARA&A, 30, 575
Condon, J. J., Condon, M. A., Gisler, G., & Puschell, J. J. 1982, ApJ, 252, 102
Condon, J. J., & Yin, Q. F. 1990, ApJ, 357, 97
Conti, P. S., & Vacca, W. D. 1993, in The Nearest Active Galaxies, ed. J. Beckman, L. Colina, & H. Netzer (Madrid: Consejo Superior de Investigaciones Cientificas), 155
———. 1994, ApJ, 423, L97
Cutri, R. M., Rudy, R. J., Rieke, G. H., Tokunaga, A. T., & Wilner, S. T. 1984, ApJ, 280, 521
DeRobertis, M. M., & Pogge, R. W. 1986, AJ, 91, 1026
Devereux, N. A., Becklin, E. E., & Scoville, N. Z. 1987, ApJ, 312, 529
Doyon, R., Joseph, R. G., & Wright, G. S. 1994, ApJ, 421, 101
Doyon, R., Puxley, P. J., & Joseph, R. D. 1992, ApJ, 397, 117
Draine, B. T. 1989, in Infrared Spectroscopy in Astronomy, ed. B. H. Kaldeich (ESA-SP 290), 93
Eckart, A., Downes, D., Genzel, R., Harris, A. I., Jaffe, D. T., & Wild, W. 1990, ApJ, 348, 434
Forbes, D. A., & Ward, M. J. 1993, ApJ, 416, 150
Fuhr, J. R., Martin, G. A., & Wiese, W. L. 1988, J. Phys. Chem. Ref. Data, 17, Suppl. 4
Gehrz, R. D., Sramek, R. A., & Weedman, D. W. 1983, ApJ, 267, 551
Genzel, R. 1992, in The Galactic Interstellar Medium, ed. D. Pfenniger & P. Bartholdi (Saas Fee 21) (Berlin: Springer), 275
Genzel, R., & Eckart, A. 1994, in Infrared Astronomy with Arrays (3), ed. I. McLean (Dordrecht: Kluwer), 433
Genzel, R., Eckart, A., Hofmann, R., Quirrenbach, A., Sams, B., & Tacconi-Garman, L. E. 1994a, Messenger, 75, 17
Genzel, R., Hollenbach, D., & Townes, C. H. 1994b, Rep. Progr. Phys., 57, 417
Genzel, R., & Townes, C. H. 1987, ARA&A, 25, 377
Grandi, S. A. 1978, ApJ, 221, 501
Greenhouse, M. A., Feldman, U., Smith, H. A., Klapisch, M., Bhatia, A. K., & Bar Shalom, A. 1993, ApJS, 88, 23
Greenhouse, M. A., Woodward, C. E., Thronson, H. A., Rady, R. J., Rossano, G. S., Erwin, P., & Puetter, R. C. 1991, ApJ, 383, 164
Güsten, R., Serabyn, E., Kasemann, C., Schinkel, A., Schneider, G., Schulz, A., & Young, K. 1993, ApJ, 402, 537
Harris, A. I., Hills, R. E., Stutzki, J., Graf, U. U., Russell, A. P. G., & Genzel, R. 1991, ApJ, 382, L75
Heckman, T. M., Beckwith, S., Blitz, L., Skrutskie, M., & Wilson, A. S. 1986, ApJ, 305, 157
Hofmann, R., Blietz, M., Duhoux, P., Eckart, A., Krabbe, A., & Rotaciuc, V. 1993, in Progress in Telescope and Instrumentation Technologies, ed. M. H. Ulrich (ESO 42) (Garching: ESO), 617
Holtzmann, J. A., et al. 1992, AJ, 103, 691
Kennicutt, R. C. 1991, in Massive Stars in Starbursts, ed. C. Leitherer et al. (Cambridge: Cambridge Univ. Press), 157
Keto, E., Ball, R., Arens, J., Jernigan, G., & Meixner, M., 1992, ApJ, 389, 223
Kleinmann, S. G., & Hall, D. N. B. 1986, ApJS, 62, 501
Korista, K. T., & Ferland, G. J. 1989, ApJ, 343, 678
Krabbe, A., et al. 1993, PASP, 105, 755
Krabbe, A., Sternberg, A., & Genzel, R. 1994, ApJ, 425, 72 (KSG)
Krolik, J. H., & Begelman, M. C. 1986, ApJ, 308, L55
Kurucz, R. L. 1979, ApJS, 40, 1
Larson, R. B., & Tinsley, B. M. 1978, ApJ, 219, 46
Lucy, L. B. 1974, AJ, 79, 745
Maeder, A., & Meynet, G. 1988, A&AS, 76, 411
Marquez, I., & Moles, M. 1994, AJ, 108, 90
Mas Hesse, J. M., & Kunth, D. 1991, A&AS, 88, 399
Mauder, W., Weigelt, G., Appenzeller, I., & Wagner, S. J. 1994, A&A, 285, 44
Mazzarella, J. M., Voit, G. M., Soifer, B. T., Matthews, K., Graham, J. R., Armus, L., & Shupe, D. 1994, AJ, 107, 1274
McLeod K. K., Rieke, G. H., Rieke, M. J., & Kelly, D. M. 1993, ApJ, 412, 111
Melnick, J., Terlevich, R., & Eggleton, P. P. 1985, MNRAS, 216, 255
Meixner, M., Puchalski, R., Blitz, L., Wright, M. C. H., & Heckman, T. M. 1990, ApJ, 354, 158
Miles, J. W., Houck, J. R., & Hayward, T. L. 1994, ApJ, 425, L37
Moorwood, A. F. M., Moneti, A., & Gredel, R. 1991, Messenger, 63, 77
Moorwood, A. F. M., & Oliva, E. 1988, A&A, 203, 278
Nussbaumer, H., & Osterbrock, D. E. 1970, ApJ, 161, 811
Oke, S., & Sargent, W. 1968, ApJ, 151, 807
Oliva, E., & Moorwood, A. F. M. 1990, ApJ, 348, L5
Oliva, E., & Origlia, L. 1992, A&A, 254, 466
Oliva, E., Salvati, M., Moorwood, A. F. M., & Marconi, A. 1994, A&A, 288, 457
Osterbrock, D. E. 1969, Astrophys. Lett., 4, 57
———. 1989, Astrophysics of Gaseous Nebulae and Active Galactic Nuclei (Mill Valley, CA: University Science)
Penston, M. V., Fosbury, R. A. E., Boksenberg, A., Ward, M. J., & Wilson, A. E. 1984, MNRAS, 208, 347
Piro, L., Yamauchi, M., & Matsuoka, M. 1990, ApJ, 360, L35
Pompea, S. M., & Rieke, G. H. 1990, ApJ, 356, 416
Reconditi, M., & Oliva, E. 1993, A&A, 274, 662
Ridgway, S. E., & Wynn-Williams, C. G. 1994, preprint
Rieke, G. H., Lebofsky, M. J., Thompson, R. I., Low, F. J., & Tokunaga, A. T. 1980, ApJ, 238, 24
Rieke, G. H., Loken, K., Rieke, M. J., & Tamblyn, P. 1993, ApJ, 412, 99
Roche, P., Aitken, D. K., Smith, C. H., & Ward, M. J. 1991, MNRAS, 248, 606
Rotaciuc, V. 1992, Ph.D. thesis, Ludwig-Maximilian-Univ. München
Rotaciuc, V., Krabbe, A., Cameron, M., Drapatz, S., Genzel, R., Sternberg, A., & Storey, J. W. V. 1991, ApJ, 370, L23
Sams, B. J., Genzel, R., Eckart, A., Tacconi-Garman, L. E., & Hofmann, R. 1994, ApJ, 430, 33
Schaerer, D., Meynet, G., Maeder, A., & Schaller, G. 1993, A&A, 174, 1012
Scoville, N. Z., Mathews, K., Carico, D. P., & Sanders, D. B. 1988, ApJ, 327, L61
Scoville, N. Z., & Soifer, B. T. 1991, in Massive Stars in Starbursts, ed. C. Leitherer et al. (Cambridge: Cambridge Univ. Press), 233
Seyfert, C. K. 1943, ApJ, 97, 28
Shields, J. 1993, ApJ, 419, 181
Shier, L. M., Rieke, M. J., & Rieke, G. H. 1994, ApJ, 433, L9
Shull, J. M., & van Steenberg, M. 1982, ApJS, 48, 95
Solomon, P., Downes, D., & Radford, S. J. E. 1992, ApJ, 398, L29
Sternberg, A., & Dalgarno, A. 1989, ApJ, 338, 197
Strong, A. W., et al. 1988, A&A, 207, 1
Tacconi, L., Genzel, R., Blietz, M., Cameron, M., Harris, A. I., & Madden, S. C. 1994, ApJ, 426, L77
Thronson, H. A., & Greenhouse, M. A. 1988, ApJ, 327, 671
Thronson, H. A., et al. 1989, ApJ, 343, 158
Thronson, H. A., Majewski, S., Descartes, L., & Hereld, M. 1990, ApJ, 364, 456
Ulvestad, J. S., Wilson, A. S., & Sramek, R. A. 1981, ApJ, 247, 419
van der Werf, P. P., Genzel, R., Krabbe, A., Blietz, M., Lutz, D., Drapatz, S., Ward, M. J., & Forbes, D. A. 1993, ApJ, 405, 522
Vazquez, E. C., & Scalo, J. M. 1989, ApJ, 343, 644
Völk, H. J. 1989, A&A, 218, 67
Walborn, N. R. 1991, in Massive Stars in Starbursts, ed. C. Leitherer et al. (Cambridge: Cambridge Univ. Press), 145
Wampler, E. J. 1971, ApJ, 164, 1
Weitzel, L. 1994, Ph.D. thesis, Ludwig-Maximilian-Univ. München
Weitzel, L., Cameron, M., Drapatz, S., Genzel, R., & Krabbe, A. 1994, in Infrared Astronomy with Arrays (3), ed. I. S. McLean (Dordrecht: Kluwer), 531
Westin, B. A. M. 1985, A&A, 151, 137
Wild, W., Harris, A. I., Eckart, A., Genzel, R., Graf, U. U., Jackson, J. M., Russell, A. P. G., & Stutzki, J. 1992, A&A, 265, 464
Wilson, A. S., Baldwin, J. A., Sun, S. D., & Wright, A. E. 1986, ApJ, 310, 121
Wilson, A. S., Helfer, T. T., Haniff, C. A., & Ward, M. J. 1991, ApJ, 381, 79